The Astrophysical Journal, 702:1321–1335, 2009 September 10 doi:10.1088/0004-637X/702/2/1321

A HEURISTIC PREDICTION OF THE COSMIC EVOLUTION OF THE CO-LUMINOSITY FUNCTIONS

D. Obreschkow, I. Heywood, H.-R. Klöckner, and S. Rawlings
Astrophysics, Department of Physics, University of Oxford, Keble Road, Oxford, OX1 3RH, UK
Received 2009 April 16; accepted 2009 July 20; published 2009 August 20

ABSTRACT

We predict the emission line luminosity functions (LFs) of the first 10 rotational transitions of $^{12}C^{16}O$ in galaxies at redshift $z = 0$ to $z = 10$. This prediction relies on a recently presented simulation of the molecular cold gas content in $\sim 3 \times 10^7$ evolving galaxies based on the Millennium Simulation. We combine this simulation with a model for the conversion between molecular mass and CO-line intensities, which incorporates the following mechanisms: (1) molecular gas is heated by the cosmic microwave background (CMB), starbursts (SBs), and active galactic nuclei (AGNs); (2) molecular clouds in dense or inclined galaxies can overlap; (3) compact gas can attain a smooth distribution in the densest part of disks; (4) CO luminosities scale with metallicity changes between galaxies; and (5) CO luminosities are always detected against the CMB. We analyze the relative importance of these effects and predict the cosmic evolution of the CO-LFs. The most notable conclusion is that the detection of regular galaxies (i.e., no AGN, no massive SB) at high $z \gtrsim 7$ in CO emission will be dramatically hindered by the weak contrast against the CMB, in contradiction to earlier claims that CMB heating will ease the detection of high-redshift CO. The full simulation of extragalactic CO lines and the predicted CO-LFs at any redshift can be accessed online (http://s-cubed.physics.ox.ac.uk/, go to "S^3-SAX") and they should be useful for the modeling of CO-line surveys with future telescopes, such as the Atacama Large Millimeter/submillimeter Array or the Square Kilometre Array.

Key words: galaxies: evolution – galaxies: high-redshift – ISM: atoms – ISM: molecules

Online-only material: color figures

1. INTRODUCTION

An increasing body of evidence suggests that molecular hydrogen (H_2) widely dominated over atomic hydrogen (H I) in the regular galaxies of the early universe (e.g., Obreschkow & Rawlings 2009a). Empirical corner stones toward this conclusion were the measurement of strong CO-line emission in distant regular galaxies (Daddi et al. 2008), the detection of H I via Lyα absorption against distant quasars (e.g., Prochaska et al. 2005), the observational confirmation of a correlation between the interstellar gas pressure and H_2/H I ratios (Blitz & Rosolowsky 2006), and the observational confirmation that galaxy sizes increase significantly with cosmic time (e.g., Bouwens et al. 2004).

In light of future millimeter/submillimeter telescopes, such as the Atacama Large Millimeter/submillimeter Array (ALMA), much attention is directed toward the possibility of detecting the suspected molecular gas (mostly H_2) at high redshift via the characteristic emission lines of the CO molecule. However, the case for frequent CO detections in regular high-redshift galaxies is by no means secure, since neither the cosmic evolution of the H_2 mass function (MF), nor the evolution of the relationship between H_2 masses and CO-line luminosities is well constrained to date. An elucidation of this situation seems nevertheless within reach, owing to a long list of specific discoveries over the past two decades (Section 3), based on which computer simulations could already predict the CO-line emission of individual high-redshift galaxies in some detail (e.g., Combes et al. 1999; Greve & Sommer-Larsen 2008). Moreover, Blain et al. (2000) and Carilli et al. (2002) predicted the number of detectable CO sources in various frequency ranges. They assumed that the CO-line luminosities evolve with the far-infrared (FIR) luminosity, and they tackled the cosmic evolution of the FIR-luminosity function (LF) by considering a pure density evolution. While this approach is perhaps justified at low redshifts, it probably oversimplifies the physical complexity of CO emission at high redshift ($z > 1$) as we shall show in this paper.

A missing jigsaw piece in the bigger picture is a physical prediction of the cosmic evolution of the galaxy LFs for different CO-emission lines. In this paper, we will attempt such a prediction by concatenating many specific empirical and theoretical findings about H_2 and CO. The two main steps toward our prediction of the CO-LFs are (1) a model for the cosmic evolution of the H_2-MF and (2) a model for the conversion between H_2 masses and CO-line luminosities. In this paper, we shall focus on the latter, while adopting the H_2 masses of a sample of $\sim 3 \times 10^7$ galaxies (Obreschkow et al. 2009), simulated based on the Millennium dark matter simulation (Springel et al. 2005).

In Section 2, we summarize the galaxy simulation producing the H_2 masses and various other galaxy properties related to CO-line emission. Our model for CO-line luminosities is developed in Section 3. Section 5 presents the prediction of the cosmic evolution of the CO-LFs and discusses their dependence on the mechanisms listed at the beginning of Section 3. Section 6 ranks the relative importance of these mechanisms and discusses the limitations of their implementation. A brief summary is given in Section 7.

2. SIMULATION OF THE H_2-MF

This section summarizes the cold gas simulation presented in Obreschkow et al. (2009). Main results and limitations were discussed in detail by Obreschkow et al. (2009) and Obreschkow & Rawlings (2009a).

The simulation has three consecutive layers. The first layer is the Millennium Simulation (Springel et al. 2005), an *N*-body dark matter simulation in a periodic box of comoving volume $(500\,h^{-1}\,\mathrm{Mpc})^3$, where $H_0 = 100\,h\,\mathrm{km\,s^{-1}\,Mpc^{-1}}$ and $h = 0.73$. The second simulation layer uses the evolving mass

skeleton of the Millennium Simulation to tackle the formation and cosmic evolution of galaxies in a semianalytic fashion (Croton et al. 2006; De Lucia & Blaizot 2007). This is a global approach, where galaxies are represented by a list of global properties, such as position, velocity, and total masses of gas, stars, and black holes. These properties were evolved using simplistic formulae for mechanisms, such as gas cooling, reionization, star formation, gas heating by supernovae, starbursts (SBs), black hole accretion, black hole coalescence, and the formation of stellar bulges via disk instabilities. The resulting virtual galaxy catalog (hereafter the "DeLucia catalog") contains the positions, velocities, merger histories, and intrinsic properties of $\sim 3 \times 10^7$ galaxies at 64 cosmic time steps. At redshift $z = 0$, galaxies as low in mass as the Small Magellanic Cloud are resolved. The free parameters in the semianalytic model were tuned to various observations in the local universe (see Croton et al. 2006). Therefore, despite the simplistic implementation and the possible incompleteness of this model, the simulated galaxies nonetheless provide a good fit to the joint luminosity/color/morphology distribution of observed low-redshift galaxies (Cole et al. 2001; Huang et al. 2003; Norberg et al. 2002), the bulge-to-black hole mass relation (Häring & Rix 2004), the Tully–Fisher relation (Giovanelli et al. 1997), and the cold gas metallicity as a function of stellar mass (Tremonti et al. 2004).

The cold gas masses of the simulated galaxies are the net result of gas accretion by cooling from a hot halo (dominant mode) and galaxy mergers, gas losses by star formation and feedback from supernovae, and cooling flow suppression by feedback from accreting black holes. The DeLucia catalog does not distinguish between molecular and atomic cold gas, but simplistically treats all cold gas as a single phase. Therefore, the third simulation layer, explained by Obreschkow et al. (2009), consists of postprocessing the DeLucia catalog to split the cold gas masses of each galaxy into H I, H_2, and He. Our model for this subdivision mainly relies on three empirical findings. (1) Most cold gas in regular spiral (Leroy et al. 2008) and elliptical galaxies (Young 2002) in the local universe resides in flat disks, and there is evidence that this feature extends to higher redshifts (e.g., Tacconi et al. 2006). (2) The surface density of the total hydrogen component (H I + H_2) is approximately described by an axially symmetric exponential profile (Leroy et al. 2008)

$$\Sigma_{\rm H}(r) = \tilde{\Sigma}_{\rm H} \exp(-r/r_{\rm disk}), \quad (1)$$

where $r_{\rm disk}$ is the exponential scale length and the normalization factor $\tilde{\Sigma}_{\rm H}$ can be calculated as $\tilde{\Sigma}_{\rm H} \equiv M_{\rm H}/(2\pi r_{\rm disk}^2)$, where $M_{\rm H}$ is the total mass of cold hydrogen in the disk. (3) The local H_2/H I mass ratio closely follows the gas pressure of the interstellar medium outside molecular clouds over at least 4 orders of magnitude in pressure and for various galaxy types (Blitz & Rosolowsky 2006; Leroy et al. 2008). Based on those findings, we (Obreschkow et al. 2009) derived an analytic expression of the H I and H_2 surface density profiles

$$\Sigma_{\rm HI}(r) = \frac{\tilde{\Sigma}_{\rm H} \exp(-r/r_{\rm disk})}{1 + R_{\rm mol}^{\rm c} \exp(-1.6\, r/r_{\rm disk})}, \quad (2)$$

$$\Sigma_{\rm H_2}(r) = \frac{\tilde{\Sigma}_{\rm H}\, R_{\rm mol}^{\rm c} \exp(-2.6\, r/r_{\rm disk})}{1 + R_{\rm mol}^{\rm c} \exp(-1.6\, r/r_{\rm disk})}, \quad (3)$$

where $R_{\rm mol}^{\rm c}$ is the H_2/H I mass ratio at the galaxy center. This model was applied to the galaxies in the DeLucia catalog to characterize their H I and H_2 content (masses, diameters, and circular velocities). The resulting hydrogen simulation successfully reproduces many local observations of H I and H_2, such as MFs, mass–diameter relations, and mass–velocity relations (Obreschkow et al. 2009). This success is quite surprising, since our model for H I and H_2 only introduced one additional free parameter to match the observed average space density of cold gas in the local universe (Obreschkow et al. 2009). A key prediction of this simulation is that the H_2/H I ratio of most regular galaxies increases dramatically with redshift, hence causing a clear signature of cosmic "downsizing" in the H_2-MF (Obreschkow & Rawlings 2009a), i.e., a negative shift in the mass scale with cosmic time.

The simulated H_2-MF at $z = 0$ approximately matches the local H_2-MF inferred from the local CO(1–0)-LF (Keres et al. 2003; Obreschkow & Rawlings 2009b), and the few measurements of CO-line emission from regular galaxies at $z \approx 1.5$ (Daddi et al. 2008) are consistent with the predicted H_2-MF at this redshift (Obreschkow & Rawlings 2009a). Furthermore, the predicted comoving space density of H_2 evolves proportionally to the observed space density of star formation rates (SFRs; e.g., Hopkins 2007) within a factor of 2 out to at least $z = 3$. For those reasons, we expect the simulated H_2-MF to scale reasonably well with redshift. Yet, at $z \gtrsim 5$ the simulation becomes very uncertain because the geometries and matter content of regular galaxies are virtually unconstrained from an empirical viewpoint. The young age and short merger intervals of these galaxies compared to their dynamical timescales, may have caused them to deviate substantially from the simplistic disk-gas model. An extended discussion of these and other limitations at low and high redshift is given in Section 6.3 of Obreschkow et al. (2009).

3. MODEL FOR THE CO/H_2 CONVERSION

Most detections of H_2 rely on emission lines originating from the relaxation of the rotational J-levels of the $^{12}C^{16}O$-molecule (hereafter "CO"). Appendix B provides background information on the inference of H_2 masses from CO-line measurements and highlights the justification and drawbacks of this method.

To predict the CO-line luminosities associated with the molecular gas masses of the simulated galaxies (Section 2), we shall now introduce a simplistic but physically motivated model for the conversion between H_2 masses and CO luminosities at any redshift. This model aims to respect the following theoretical and empirical constraints.

1. The temperature of molecular gas depends on the temperature of the cosmic microwave background (CMB) and on the radiative feedback from SBs and active galactic nuclei (AGNs).
2. Molecular clumps can shield each other if they overlap along the line of sight and in velocity space. This effect may not be negligible in the dense galaxies at high redshift, especially if observed edge-on.
3. While locally observed molecular gas is organized in giant molecular clouds (GMCs), the dense gas in compact luminous galaxies, such as ultraluminous infrared galaxies (ULIRGs), is predicted to follow a smooth distribution.
4. The CO-line emission of molecular gas is correlated with the CO/H_2 mass ratio, i.e., to the metallicity of the galaxy.
5. The CMB presents an observing background. The absorption of CO lines against the CMB may significantly reduce the effectively detectable luminosities of CO-emission lines.

These mechanisms will be modeled one by one over Sections 3.1–3.5.

3.1. Gas Temperature and the CO Ladder

To model the luminosity ratios of different CO lines, we analyzed the CO spectral energy distributions (SEDs) of nine galaxies drawn from the literature (see Figure 1 and references therein). This sample includes local regular galaxies, local and distant SBs, and distant quasi-stellar objects (QSOs). Four of these sources (SMM J16359+6612, F10214+4724, APM 08279+5255, Cloverleaf H1413+135) are known to be strongly magnified by gravitational lensing. We assume that this has no major effect on the flux ratios between different CO lines. This assumption relies on the fact that the lensed galaxies are FIR-bright objects, which makes it likely that the strongly lensed regions include the star-bursting ones. Those are also the high-excitation (HE) regions, which seem to dominate the CO emission of most CO lines (see discussion of M 82 in this section).

Surprisingly, all nine CO-SEDs are well fitted by a model for a single gas component in local thermodynamic equilibrium (LTE). In Appendix C, we show that the frequency-integrated line luminosities (=power) of such a model scales with the upper level J of the transition as

$$L_J \propto \left[1 - \exp(-\tau_J)\right] \cdot \frac{J^4}{\exp\left(\frac{h_\mathrm{p}\,\nu_\mathrm{CO}\,J}{k_\mathrm{b}\,T_\mathrm{e}}\right) - 1}, \qquad (4)$$

where T_e is the excitation temperature, $\nu_\mathrm{CO} = 115\,\mathrm{GHz}$ is the rest-frame frequency of the CO(1–0)-transition, and τ_J is the optical depth. The latter scales with J as

$$\tau_J = 7.2\,\tau_\mathrm{c}\,\exp\left(-\frac{h_\mathrm{p}\,\nu_\mathrm{CO}\,J^2}{2\,k_\mathrm{b}\,T_\mathrm{e}}\right)\sinh\left(\frac{h_\mathrm{p}\,\nu_\mathrm{CO}\,J}{2\,k_\mathrm{b}\,T_\mathrm{e}}\right), \qquad (5)$$

where τ_c is a constant. The factor 7.2 in Equation (5) was introduced in order for τ_c to correspond to the optical depth of the CO(1–0) line (i.e., $\tau_1 = \tau_\mathrm{c}$) at the excitation temperature $T_\mathrm{e} \approx 17\,\mathrm{K}$, which is the lowest temperature of our model (see the end of this section).

If normalized to the CO(1–0) luminosity L_1, the LTE model of Equations (4) and (5) has two free parameters τ_c and T_e. In order to apply this model to the velocity-integrated fluxes S^V_J shown in Figure 1, we use the relation $L_J \propto J\,S^\mathrm{V}_J$ (see Appendix A, Equation (A15)).

We first fitted the LTE model to the observed CO-SEDs individually via χ^2-minimization. The resulting 1σ confidence intervals of the temperatures T_e equal 10%–20% of their best-fit values. Despite this uncertainty, a clear dependence of T_e on the galaxy types (regular, SB, QSO) can de detected (see below). By contrast, the parameters τ_c are poorly constrained. Their best-fit values range from 0.5 to 5 with no clear trend amongst the different galaxy types, and their confidence intervals are such that a single parameter τ_c for all CO-SEDs seems to provide a consistent solution. We therefore tested a second model, where all nine SEDs share the same parameter τ_c, and found that the Bayesian evidence (e.g., Sivia & Skilling 2006) of this 10-parameter model ($1 \times \tau_\mathrm{c}$, $9 \times T_\mathrm{e}$) against the 18-parameter model ($9 \times \tau_\mathrm{c}$, $9 \times T_\mathrm{e}$) is "strong" with odds of order 10^5:1. We therefore assume a single parameter τ_c for all galaxies, emphasizing, however, that the actual optical depth τ_J varies considerably as a function of J and T_e by virtue of Equation (5). The best fit to all nine SEDs yields $\tau_\mathrm{c} = 2$, consistent with the moderate optical depths for different CO lines found by Barvainis et al. (1997) in the Cloverleaf quasar. The excitation temperatures T_e corresponding to $\tau_\mathrm{c} = 2$ are listed in Figure 1. The individual reduced χ^2's for each galaxy range from 0.5 to 1.2, hence demonstrating that the LTE model with a single parameter τ_c provides an excellent fit to all observed CO-line ratios.

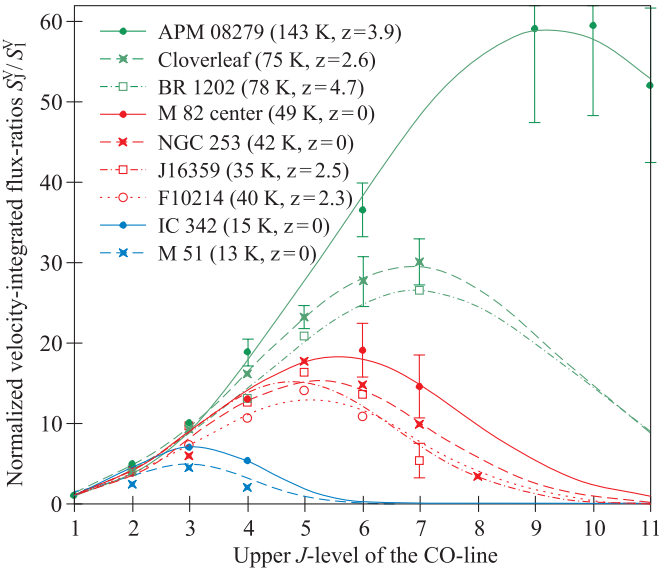

Figure 1. CO-SEDs of nine nearby and distant galaxies: APM 08279+5255 (Weiss et al. 2007), Cloverleaf H1413+117 (Barvainis et al. 1997), BR 1202-0725 (Omont et al. 1996; Kawabe et al. 1999), the central region of M 82 (Weiss et al. 2005b), NGC 253 (Güsten et al. 2006), SMM J16359+6612 (Weiss et al. 2005a), IRAS F10214+4724 (Ao et al. 2008), IC 342 (Israel & Baas 2003), and M 51 (Wielebinski et al. 1999; Nieten et al. 1999). Symbols and error bars represent the measurements, but to avoid confusion, only some error bars are displayed. The lines represent fits of our model for thermalized gas with finite optical depth, and the corresponding excitation temperatures T_e are indicated for each galaxy. Different colors are used for regular galaxies (blue), SBs (red), and QSOs (green).

This conclusion justifies the use of the single component LTE model as a *working model*, but it does not imply that this model describes the *physical reality* of molecular gas. In fact, it seems that neither the assumption of LTE conditions, nor that of a single gas component are fully satisfied in reality.

First, the density of molecular gas is often too low to collisionally excite the higher rotational levels to thermal equilibrium. In this case, the LTE conditions are not met. A more accurate description of the excitation state is then provided by the so-called large velocity gradient (LVG) models (de Jong et al. 1975), which are more complex than the LTE model. A plausible explanation for the surprising success of the LTE model is that the suppression of high-J emission by subthermal excitation can be approximately mimicked by a thermalized gas with a slightly underestimated optical depth, or a temperature T_e slightly below the kinetic temperature of the gas. Another explanation is that in real clouds the subthermal excitation of high-J states could be compensated by a minor fraction of much warmer (~100 K) and denser molecular gas, such as is seen next to the star-forming cores in nearby molecular clouds (e.g., the "ridge" in the Orion molecular cloud; Lis & Schilke 2003). In any case, we stress that the temperatures T_e identified by our LTE analysis should not be considered as very accurate. Better

models, albeit more complex, can be found in the references of Figure 1.

Second, the assumption of a single component seems to work because in most galaxies one component widely dominates the total CO-SED. A good example to illustrate this conclusion and its limitations is the nearby SB M 82, for which the CO-SED up to the CO(7–6) transition has been presented by Weiss et al. (2005b). The CO-SED of the center of M 82 is displayed in Figure 1 and is reasonably well described by a LTE model (reduced $\chi^2 = 1.1$). Yet, an in-depth LVG analysis (Figure 7 in Weiss et al. 2005b) revealed that the center of M 82 exhibits a low-excitation (LE) and an HE component with kinetic temperatures of ∼50 K (perhaps higher for the LE component), consistent with the single temperature of the LTE model of 49 K (see Figure 1). In terms of velocity-integrated fluxes, the CO-SED of the LE component peaks around the upper level $J = 3$–4, while the HE component peaks around $J = 6$–7. However, the flux from the HE component completely dominates the combined CO-SED, such that the latter still peaks around $J = 6$–7. This domination of the HE component justifies the use of a single component as a working model. Moreover, the domination of the HE component, in which the excitation conditions are close to LTE, adds another reason for the aforementioned success of the LTE model. The limitations of the single component model become obvious, when considering the CO-SED of the entire galaxy M 82 (Weiss et al. 2005b). The exceptionally strong gas outflows from the star-bursting center add an additional LE component, which dominates the total CO-SED up to the CO(3–2) transition or perhaps the CO(4–3) transition. The success of the single component model for the other three SBs in Figure 1 suggests that the strongly CO luminous outflows of M 82 are rather anomalous.

Despite the above limitations of the single component LTE model, we shall use this model for the rest of this paper for three reasons: (1) given current computational resources, applying an LVG model to $\sim 10^9$ galaxies (i.e., up to $\sim 3 \times 10^7$ galaxies per discrete time step) is highly impractical; (2) as demonstrated above (e.g., Figure 1), the LTE model is a reasonable working model in the sense that it can approximately fit most observed CO-SEDs; and (3) the differences between the LTE model and the LVG model are often much smaller than the uncertainties associated with other mechanisms, such as cloud overlap in high-z galaxies, metallicity, or gas heating by SBs (see Section 6.2).

Figure 1 demonstrates that the characteristic excitation temperatures T_e increase from regular galaxies to SBs, and more so to QSOs. This supports the interpretation of gas heating by radiation from SBs and AGNs (see also observations of Weiss et al. 2007 and theoretical work of Maloney & Black 1988). On the other hand, T_e must also depend on the temperature of the CMB at the redshift of the source (Silk & Spaans 1997; Combes et al. 1999).

We assume that in regular galaxies the molecular gas is heated by a constant specific power (i.e., power per unit gas mass), representing the intracloud radiative heating by massive stars and supernovae associated with regular star formation efficiencies. This specific power implies a minimal temperature T_0 for the bulk of the molecular gas. In addition, the CMB represents a background temperature of $T_{CMB}(z) = (1+z) \cdot 2.7\,K$. If the radiative heating of molecular gas happens via absorption by optically thick dust, then the resulting gas temperature or the CO excitation temperature is $T_e^4 \approx T_0^4 + T_{CMB}(z)^4$, as can be seen from combining the Stefan–Boltzmann law with the conservation of energy. Following the same argument, we can also include the heating of SBs and AGNs via

$$T_e^4 = T_0^4 + T_{CMB}^4(z) + T_{SB}^4 + T_{AGN}^4, \quad (6)$$

where T_{SB} and T_{AGN} are galaxy-dependent parameters characterizing the estimated temperatures of the molecular gas, if, respectively, SB feedback or AGN feedback were the only sources of radiative heating. Combes et al. (1999) pointed out that, if the radiative transfer is mediated by optically thin dust with an optical depth proportional to λ^{-2}, the exponents in Equation (6) should be increased from 4 to 6. In reality, the exponents in Equation (6) are therefore likely to be somewhat higher than 4. Yet, Equation (6) only depends on the precise value of the exponents in the few cases where the highest temperatures on the right-hand side are comparable, while otherwise the highest temperature completely dominates T_e.

In the following, we require that the specific radiation power ($\propto T_{SB}^4$) acquired by the molecular gas from SBs, increases proportionally to the surface density of the SFR Σ_{SF} for small values of Σ_{SF}, while saturating at an upper limit, characterized by the temperature T_{SB}^{max}. This saturation level encodes all possible self-regulation mechanisms, preventing further heating, such as the suppression of star formation by photodissociation of molecular gas. To parameterize the efficiency of SB heating, we define the characteristic SFR density Σ_{SF}^c, at which the specific radiation power reaches 50% of the saturation level. A minimal parameterization of these requirements is given by the function

$$T_{SB}^4 = T_{SB}^{max\,4}\,\Sigma_{SF}/(\Sigma_{SF} + \Sigma_{SF}^c), \quad (7)$$

which reduces to the linear relation $T_{SB}^4 \approx T_{SB}^{max\,4}\,\Sigma_{SF}/\Sigma_{SF}^c$ for $\Sigma_{SF} \ll \Sigma_{SF}^c$. To compute $\Sigma_{SF} = SFR/(\pi\, r_{SF}^2)$ for the galaxies in our simulation, we approximate the characteristic length r_{SF} with the half-mass radius $r_{H_2}^{half}$ of molecular gas and we use the SFRs computed by the semianalytic model (see Croton et al. 2006). In this model, stars can form via two mechanisms: (1) quiescent continual star formation in the disk, which depends on the cold gas surface density and (2) star-bursting activity in the bulge, which is driven by galaxy mergers. We shall use the combined SFRs of both modes to calculate Σ_{SF}, since, in principle, both modes are likely to cause intercloud radiative heating, if the corresponding SFR densities are high enough, i.e., of order Σ_{SF}^c.

In analogy to SBs, we parameterize the heating from AGNs via

$$T_{AGN}^4 = T_{AGN}^{max\,4}\,\dot{M}_{BH}/(\dot{M}_{BH} + \dot{M}_{BH}^c), \quad (8)$$

where T_{AGN}^{max} is the maximal CO excitation temperature that can be achieved by AGN heating, $\dot{M}_{BH}$ is the black hole mass accretion rate, and $\dot{M}_{BH}^c$ is the critical accretion rate, where the specific heating power is half the maximum value. In the semianalytic model of the DeLucia catalog (Croton et al. 2006), black holes can grow via two mechanisms: (1) a quiescent mode, whereby black holes continually accrete material from a static hot halo and (2) a merger mode, where the black holes of merging galaxies coalesce, while accreting additional material from the cold gas disks. The free parameters in this model were adjusted such that the predicted relation between black hole mass and bulge mass matches the local observations by Häring & Rix (2004). Since our model for CO heating only depends on $\dot{M}_{BH}$, we have implicitly assumed that all growing black holes have the same heating efficiency, independent of their

growth mode and physical parameters, such as the black hole mass—a simplistic assumption, which may well require a more careful treatment as large samples of CO-detected AGN become available.

To finalize our model, we need to estimate the five parameters T_0, $T_{\rm SB}^{\rm max}$, $T_{\rm AGN}^{\rm max}$, $\Sigma_{\rm SF}^{\rm c}$, and $\dot{M}_{\rm BH}^{\rm c}$. To fix T_0, we consider regular galaxies (no SB, no AGN) in the local universe ($T_{\rm CMB}(z = 0) = 2.7\,{\rm K}$), where Equation (6) implies that $T_{\rm e}$ is nearly identical to T_0. From simultaneous CO(2–1) and CO(1–0) detections in 35 regular galaxies in the local universe, Braine et al. (1993) concluded that the ratio between the brightness temperature luminosities is $L_2^{\rm T}/L_1^{\rm T} = 0.89$ with a scatter of only 0.06. According to Equation (A13), this is equivalent to $L_2/L_1 = 2^3 \times 0.89$, which, by virtue of Equations (4) and (5), implies a one-to-one correspondence between $T_{\rm e} \approx T_0$ and $\tau_{\rm c}$. If we impose $\tau_{\rm c} = 2$ (see above), then $T_0 \approx 17\,{\rm K}$, which roughly agrees with the excitation temperatures of the regular galaxies M 51 and IC 342 for the same depth parameter (see Figure 1). We therefore fix $T_0 \equiv 17\,{\rm K}$.

We further set the critical star formation density to $\Sigma_{\rm SF}^{\rm c} \equiv 500\,M_\odot\,{\rm yr}^{-1}\,{\rm kpc}^{-2}$, consistent with observations of the nuclear SBs of M 82 (de Grijs 2001) and NGC 253 (Beck & Beckwith 1984). For those galaxies, Equation (7) then implies that $T_{\rm SB}^{\rm max\,4} = T_{\rm SB}^4/2$, where $T_{\rm SB} \approx T_{\rm e} = 40$–$50\,{\rm K}$ (see Figure 1), hence $T_{\rm SB}^{\rm max} = 50$–$60\,{\rm K}$. We therefore choose $T_{\rm SB}^{\rm max} \equiv 60\,{\rm K}$. Our chosen value for $\Sigma_{\rm SF}^{\rm c}$ also compares well to the star formation density $\sim 10^3\,M_\odot\,{\rm yr}^{-1}\,{\rm kpc}^{-2}$ predicted by Thompson et al. (2005) for the optically thick, dense regions of star-forming disks.

For AGN heating, we choose $T_{\rm AGN}^{\rm max} \equiv 150\,{\rm K}$, assuming that the QSO APM 08279+5255 represents an object close to the maximal possible heating. The critical black hole accretion rate $\dot{M}_{\rm BH}^{\rm c}$ is assumed to be $\dot{M}_{\rm BH}^{\rm c} \equiv 10\,M_\odot\,{\rm yr}^{-1}$, consistent with the higher Eddington accretion rates in the sample of 121 radio-loud quasars studied by Bao et al. (2008). Assuming a standard radiative accretion efficiency of 10%, this value for $\dot{M}_{\rm BH}^{\rm c}$ corresponds to a black hole mass of $5 \times 10^8\,M_\odot$, which is on the order of a typical progenitor of the supermassive black holes found in the massive galaxies in the local universe.

3.2. Overlap of Molecular Clumps

A reason, why CO radiation can be used as a *linear* tracer of molecular mass in nearby galaxies despite its optical thickness is that most lines of sight to the molecular clumps in nearby galaxies do not cross other clumps, and hence CO behaves as if it were optically thin (see Appendix B). However, at high redshift, galaxies are denser (e.g., Bouwens et al. 2004) and carry more molecular gas (Obreschkow & Rawlings 2009a), and thus the overlap (in space and velocity) of molecular clumps may become significant. Such overlap will (1) reduce the directly visible surface area per unit molecular mass and (2) increase the effective optical depth of the CO radiation.

Bally et al. (1987; see also Genzel & Stutzki 1989) identified and analyzed more than 100 clumps in the Orion molecular cloud. Based on these data, we assume that the diameters and masses of clumps are approximately $r_{\rm clump} = 1\,{\rm pc}$ and $M_{\rm clump} = 500\,M_\odot$. Given a total molecular mass $M_{\rm H_2}$, the number of clumps is approximated by

$$N = \frac{M_{\rm H_2}}{M_{\rm clump}} \tag{9}$$

and the "fractional filling factor" of a single clump can be approximated as

$$\kappa = \frac{0.1\,r_{\rm clump}^2}{q_{\rm H_2}\,r_{\rm H_2}^2}, \tag{10}$$

where $q_{\rm H_2}$ is the axes ratio of the inclined galaxy disk[1] as seen by the observer and $r_{\rm H_2}$ is the radius of molecular gas in this disk, which we take as the galactocentric radius, where $\Sigma_{\rm H_2}(r)$ given in Equation (3) equals 10% of the maximal surface density. The factor 0.1 accounts for the fact that clouds are only considered to "overlap," if they have comparable radial velocities, as otherwise they become mutually transparent to CO-line radiation. The value of 0.1 is a rough estimate based on the velocity dispersion of each clump (1–10 km s^{-1}; Bally et al. 1987; Maddalena et al. 1986) and the fact that the relative velocities between two clumps can vary from 10 km s^{-1} (if in the same cloud complex) up to the circular velocity of the disk of several 100 km s^{-1} (if in different parts of the galaxy). In a more accurate model, the value 0.1 would have to be altered with the inclination of the galaxy.

Assuming that the clumps are randomly distributed in space and frequency, we find that the fractional volume of the position–velocity space covered by the N clumps, counting overlapping regions only once, is

$$F = 1 - (1 - \kappa)^{\rm N}. \tag{11}$$

$F \in [0, 1]$ is here called the "filling factor" (although other definitions of this term exist) and its expression of Equation (11) can be derived iteratively by realizing that the filling factor of i clumps, $i > 1$, is $\kappa_{\rm i} = \kappa_{\rm i-1} + \kappa(1 - \kappa_{\rm i-1})$ with $\kappa_1 \equiv \kappa$. Since the summed volume occupied by all clumps in the position–velocity space equals $N\,\kappa$, we find that any line-of-sight crossing at least one clump must on average cross

$$B = \frac{N\,\kappa}{1 - (1 - \kappa)^{\rm N}}. \tag{12}$$

clumps, which also overlap in velocity space. If clumps do not overlap (i.e., $B = 1$), the emergent CO-line luminosities are proportional to the number of clumps N, and hence proportional to the molecular mass $M_{\rm H_2}$ (see Equation (9)). However, if the clumps overlap (i.e., $B > 1$), the directly visible surface area of the molecular gas is proportional to $M_{\rm H_2}/B$ and the optical depth increases from τ_J to $B\,\tau_J$.

3.3. Clumpy and Smooth Molecular Gas

Measurements of CO-emission lines in distant ULIRGs revealed that the use of CO-luminosity-to-H_2-mass conversion factors known from local galaxies leads to H_2 masses on the order of or larger than the dynamical masses inferred from the circular velocities (Scoville et al. 1991; Solomon & Vanden Bout 2005). This contradiction and high-resolution CO maps of ULIRGs led to the new understanding that the densely packed GMCs at the center of massive compact galaxies are unstable against the tidal shear and therefore disintegrate into a smooth blend of gas and stars. Detailed observations and geometrical models of Downes et al. (1993) and Downes & Solomon (1998) uncovered that the smooth gas is about five times more CO luminous per unit molecular mass. Multiple line observations of the two nearby ULIRGs Arp 220 and NGC 6240 (Greve et al. 2009, and references therein) seem to confirm this model, but

[1] The simulated DeLucia catalog does not provide galaxy orientations. We therefore assign inclinations randomly between 0° (face-on) and 90° (edge-on) according to a sine distribution.

they also demonstrate that gas in the dense phase may coexist with less dense gas enveloping the dense nuclear disk.

To account for the possibility of smooth molecular gas, we assume that CO luminosities per unit molecular mass scale proportionally to the efficiency

$$\varepsilon = f_{\rm clumpy} + 5 \cdot (1 - f_{\rm clumpy}), \quad (13)$$

where $f_{\rm clumpy}$ is the H_2 mass fraction in the regular clumpy phase (i.e., in GMCs) and $(1 - f_{\rm clumpy})$ is the H_2 mass fraction in the regular phase. We define the transition between the clumpy and the smooth gas phase at the H_2 surface density threshold $\Sigma_{\rm c} = 10^3\, M_\odot\, {\rm pc}^{-2}$, which is between the highest H_2 densities observed in the local universe ($\sim 10^2\, M_\odot\, {\rm pc}^{-2}$, e.g., NGC 6946; Leroy et al. 2008) and the most extreme H_2 surface densities of ULIRGs ($\sim 10^4\, M_\odot\, {\rm pc}^{-2}$, e.g., Arp 220 and NGC 6240; Greve et al. 2009). Assuming a thickness of the nuclear disk of a few 10 pc, consistent with the nuclear disk model of Downes & Solomon (1998), the adopted value of value of $\Sigma_{\rm c}$ corresponds to a volume density of $\gtrsim 10^3\, {\rm cm}^{-3}$. This value falls in between the two volume densities found by Greve et al. (2009) for the smooth and dense gas phases of Arp 220 and NGC 6240.

In the smooth phase, the H_2/H I mass ratio is much larger than unity, so that the H_2 surface density $\Sigma_{\rm H_2}(r)$ can be safely approximated by the total hydrogen density $\Sigma_{\rm H}(r)$ given in Equation (1). The H_2 mass fraction in regions less dense than $\Sigma_{\rm c}$, can then be calculated as

$$f_{\rm clumpy} = \begin{cases} \frac{\Sigma_{\rm c}}{\tilde{\Sigma}_{\rm H}} \left[1 + \ln\left(\frac{\tilde{\Sigma}_{\rm H}}{\Sigma_{\rm c}} \right) \right] & {\rm if} \tilde{\Sigma}_{\rm H} > \Sigma_{\rm c}, \\ 1 & {\rm otherwise.} \end{cases} \quad (14)$$

We shall assume that the overlap factor B is calculated in the same way for the smooth component as for the clumpy one, which corresponds to approximating the self-shielding of the smooth region by the self-shielding of a densely packed distribution of clumps with the same total volume and mass.[2] Figure 2 shows the simulated global fraction of H_2 mass in the smooth phase and the fraction of CO power from this phase as a function of cosmic time. The predicted monotonic increase of both fractions with redshift clearly reflects the strong density and size evolution of cold gas disks predicted by the simulation.

At $z = 2$, the H_2 mass fraction in the smooth phase is about 0.3% (corresponding to a fractional CO power of $\sim$1%), roughly consistent with the fact that the space density of ULIRGs is $\sim$1% of the space density of normal galaxies at this redshift (Daddi et al. 2008). The remaining 99% of CO power at $z = 2$ in the simulation stems from clumpy gas, i.e., from GMCs. This result seems consistent with recent observational evidence that star formation in many active star-forming galaxies at $z \approx 2$ is distributed on significantly larger scales than in ULIRGs (Daddi et al. 2008; Genzel et al. 2008) and that star formation properties in high-z galaxies are similar to those in GMCs (e.g., Gao 2009).

At $z = 5$, the CO power from the smooth gas phase is predicted to make up $\sim$10% of the total CO power of all galaxies. One might argue that such small fractions can be neglected. However, in Section 5.2, we will show that the contribution of CO radiation from smooth molecular gas at $z = 5$ will change the space density of the brightest objects in the CO-LFs by an order of magnitude.

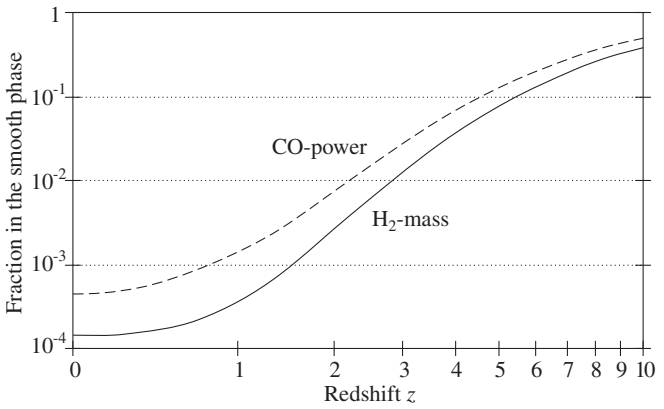

Figure 2. Cosmic evolution of the H_2 mass fraction in the smooth gas phase summed over all galaxies in the simulation (solid line), and the corresponding fraction of CO-line power (dashed line).

3.4. Metallicity

Various recent observations revealed significant variations of the CO-luminosity-to-H_2-mass conversion factor within and amongst the Milky Way (MW) and several nearby galaxies (Arimoto et al. 1996; Boselli et al. 2002; Wilson 1995; Israel 2000). In general, the CO luminosity per unit molecular mass turned out to be roughly proportional to the mass fraction of metals (Obreschkow & Rawlings 2009b). Such a dependence may naively be expected for radiation emitted by a metallic[3] molecule like CO, but considering the optical thickness of this radiation, one could also conclude that the CO luminosity per unit molecular mass is nearly independent of the metallicity (Kutner & Leung 1985). However, lower metallicities imply a lower dust-to-gas ratio and hence a more efficient destruction of CO by ultraviolet (UV) radiation, which can restore a positive correlation between metallicities and the CO luminosities (see Maloney & Black 1988, and references therein).

Based on these quantitative measurements and qualitative theoretical considerations, we decided to scale the luminosity of all CO lines proportionally to $Z \equiv M_{\rm Z}/M_{\rm gas}$, where $M_{\rm Z}$ is the metal mass in cold gas and $M_{\rm gas}$ is the total cold gas mass (including He).

3.5. Effective Luminosity Against the CMB

The CMB power per unit frequency has its maximum within the frequency band covered by the CO lines. For example, at $z = 0$ the CMB peaks between the CO(1–0) line and the CO(2–1) line, and at $z = 5$ the CMB peaks between the CO(8–7)-line and the CO(9–8) line. Therefore, the absorption of CO lines against the CMB may significantly reduce the detectable luminosities of CO-emission lines.

Within our assumption that clouds are in local thermal equilibrium (LTE), Kirchhoff's law of thermal radiation globally predicts that the absorptivity of the clouds equals their emissivity. Explicitly, if a cloud emitting thermal radiation with a power per unit frequency equals to $\epsilon(\nu)\, u(\nu, T_{\rm e})$, where $\epsilon(\nu) \in [0, 1]$ is the emissivity at the frequency ν and $u(\nu, T_{\rm e})$ is the power per unit frequency of a blackbody, then the absorbed CMB power per unit frequency equals $\epsilon(\nu)\, u(\nu, T_{\rm CMB})$. The effective CO-line luminosity measured against the CMB is the difference between the intrinsic luminosity emitted by the source and the luminosity absorbed from the CMB. If the intrinsic luminosity of the source

[2] The filling factor F of the smooth component turns out to be very close to 1, and hence $B \approx N\kappa$.

[3] Here, all elements other than hydrogen and helium are referred to as "metals."

is proportional to Equation (4), the effective luminosity against the CMB can be obtained by replacing the second factor (i.e., the blackbody factor) in Equation (4) by

$$\ell(J, T_e, z) \equiv \frac{J^4}{\exp\left(\frac{h_p \nu_{CO} J}{k_b T_e}\right) - 1} - \frac{J^4}{\exp\left(\frac{h_p \nu_{CO} J}{k_b T_{CMB}(z)}\right) - 1}. \quad (15)$$

In particular, this expression ensures that no radiation can be detected from molecular gas in thermal equilibrium with the CMB, since $\ell(J, T_{CMB}(z), z) = 0$. Alternatively, Equation (15) could also be expressed in terms of brightness temperatures (e.g., Equation (14.46) of Rohlfs & Wilson 2004).

4. COMBINED MODEL FOR CO-LINE LUMINOSITIES

A priori, we departed from the idea that CO-line fluxes L_J scale with the total mass of molecular hydrogen M_{H_2}. Combining this assumption with the models of Sections 3.1–3.5, we heuristically suggest that the CO-line luminosity (power) of the transitions $J \rightarrow J-1$ is given by

$$L_J = M_{H_2} \cdot \frac{k\, Z\, \varepsilon}{B} \cdot \left[1 - e^{-B\,\tau_J}\right] \cdot \ell(J, T_e, z), \quad (16)$$

where k is an overall normalization factor. Consistent with common practice, we shall define k in such a way that L_J is the line power, obtained by integrating the power per unit solid angle emitted along the line of sight over all directions, even though the emission need not be isotropic. In fact, our model is explicitly nonisotropic, since the parameter B depends on the inclination of the galaxy via the axes ratio q_{H_2}.

To estimate the value of k, we note that in local regular galaxies all molecular gas is in the clumpy phase (i.e., $\varepsilon = 1$), molecular clumps barely overlap (i.e., $B = 1$), and the excitation temperatures are given by $T_e \approx T_0$, hence $\tau_J = \tau_c = 2$ and $\ell(1, T_e, 0) = 2.45$. Therefore, Equation (16) for $J = 1$ reduces to

$$L_1 = 2.12\, k\, Z\, M_{H_2}. \quad (17)$$

According to Equation (17), k is proportional to the standard CO/H_2 conversion factor α_1 (Appendix B); in fact, combining Equation (17) with Equations (B2) and (A13) yields $k = 11.9\, k_b\, f co^3\, Z^{-1}\, c^{-3}\, \alpha_1^{-3}$. Adopting the value $\alpha_1 = 4.6\, M_\odot (\mathrm{K\ km\ s^{-1}\ pc^2})^{-1}$, typical for the MW (Solomon & Vanden Bout 2005), and a cold gas metallicity of $Z = 0.01$–0.02, yields $k = (5 - 10) \times 10^{-8}\, \mathrm{W\, kg^{-1}}$.

Here, we shall fix the parameter k such that Equation (16) applied to the H_2 masses of our simulated galaxies (Section 2) at $z = 0$ reproduces the observed CO(1–0) LF of the local universe as measured by Keres et al. (2003, see Figure 3). A χ^2-minimization for the luminosity range $L_1 > 10^{5.5}\, \mathrm{Jy\, km\, s^{-1}\, Mpc^2}$, i.e., the range where our simulated H_2-MF is complete, yields

$$k = 8 \times 10^{-8}\, \mathrm{W\, kg^{-1}}, \quad (18)$$

which is indeed consistent with the aforementioned value predicted from the CO/H_2 conversion of the MW.

5. RESULTS

We have applied the model of Equation (16) to the galaxies of the hydrogen simulation described in Section 2. The predicted CO-LFs for the first 10 rotational transitions in the redshift range $z = 0$–10 are displayed in Figure 3. For consistency with observer's practice, the luminosity scales refer to velocity-integrated luminosities L^V, as opposed to the frequency-integrated luminosities L (=power) used in Section 3. The conversion between those luminosities depends on the wavelength of the emission line as explained in Appendix A.

The good match (reduced $\chi^2 = 0.7$) between the simulated CO(1–0) LF at $z = 0$ and the local CO(1–0) LF, inferred by Keres et al. (2003) from FIR-selected sample of *IRAS* galaxies, is due to our tuning of the constant k and the reasonably accurate H_2 mass distribution of our hydrogen simulation (Section 2).

The simulation shows a clear signature of cosmic downsizing from $z = 2$ to $z = 0$ for all CO transitions. This feature reflects the predicted downsizing of H_2 masses (Obreschkow & Rawlings 2009a). For the particular case of the CO(2–1) LF at $z = 2$, the simulation result is roughly consistent with the space density (open circle in Figure 3) inferred from two recent CO(2–1) emission measurements in normal galaxies at $z = 1.5$ by Daddi et al. (2008). We note that the offset of this empirical data point from our simulation is larger in Figure 3 than in Figure 1 of Obreschkow & Rawlings (2009a). In the latter, we have compared the empirical data point of Daddi et al. (2008) to our simulated H_2-MF at $z = 2$. To this end, we converted the measured CO(2–1) luminosities into H_2 masses using the standard CO/H_2 conversion factor for ULIRGs, $\alpha_2 = 1\, M_\odot (\mathrm{K\ km\ s^{-1}\ pc^{-2}})^{-1}$ (Daddi et al. 2008; see definition of α_2 in Appendix B). However, the model for the CO/H_2 conversion of this paper yields higher values of α_2 for regular high-redshift galaxies, such as those found by Daddi et al. (2008).

For higher order transitions ($J > 5$), the predicted downsizing even extends out to $z \approx 5$, due to the strong dependence of these transitions on SBs and AGNs (Section 5.1). In Figure 3, the "dominant" transition, i.e., the one with the maximal velocity-integrated luminosity per unit cosmic volume, is indicated at each redshift. The upper J-level of this transition increases with redshift due to the combined radiative heating by SBs and AGNs. We shall now analyze the dependence of the CO-LFs on the individual mechanisms modeled in Section 3.

5.1. Effects of Radiative Heating by SBs and AGNs

Figure 4 compares the simulated CO(1–0) LF and CO(6–5) LF at $z = 0$ and $z = 8$ to the corresponding LFs, if either AGN heating or SB heating is suppressed. At low redshift, both SBs and AGNs have nearly no observable effect on the CO(1–0) LF, consistent with the conclusion of Keres et al. (2003) that only the highest luminosity bin of the measured CO(1–0) LF could indicate a deviation from a Schechter function distribution, perhaps due to SBs in the sample.

By contrast, the CO(6–5) LF appears to be significantly boosted by AGNs at $z = 0$. In fact, this simulated LF deviates from a Schechter function and exhibits two "knees," respectively, corresponding to a "normal" galaxy population (left knee) and a more luminous population heated by AGNs (right knee). Since the luminous end of the CO(6–5) LF is entirely dominated by AGN heating, we expect the local space density of the most CO(6–5) luminous objects to match the space density of local AGNs. To test the simulation, we therefore overlaid the simulated local CO(6–5) LF with the most recent empirical determination of the local hard (2–8 keV) X-ray LF (HX LF) obtained by Yencho et al. (2009; data points in Figure 4, top). This HX LF relies on a galaxy sample studied by the *Chandra X-Ray Observatory*. In order to map

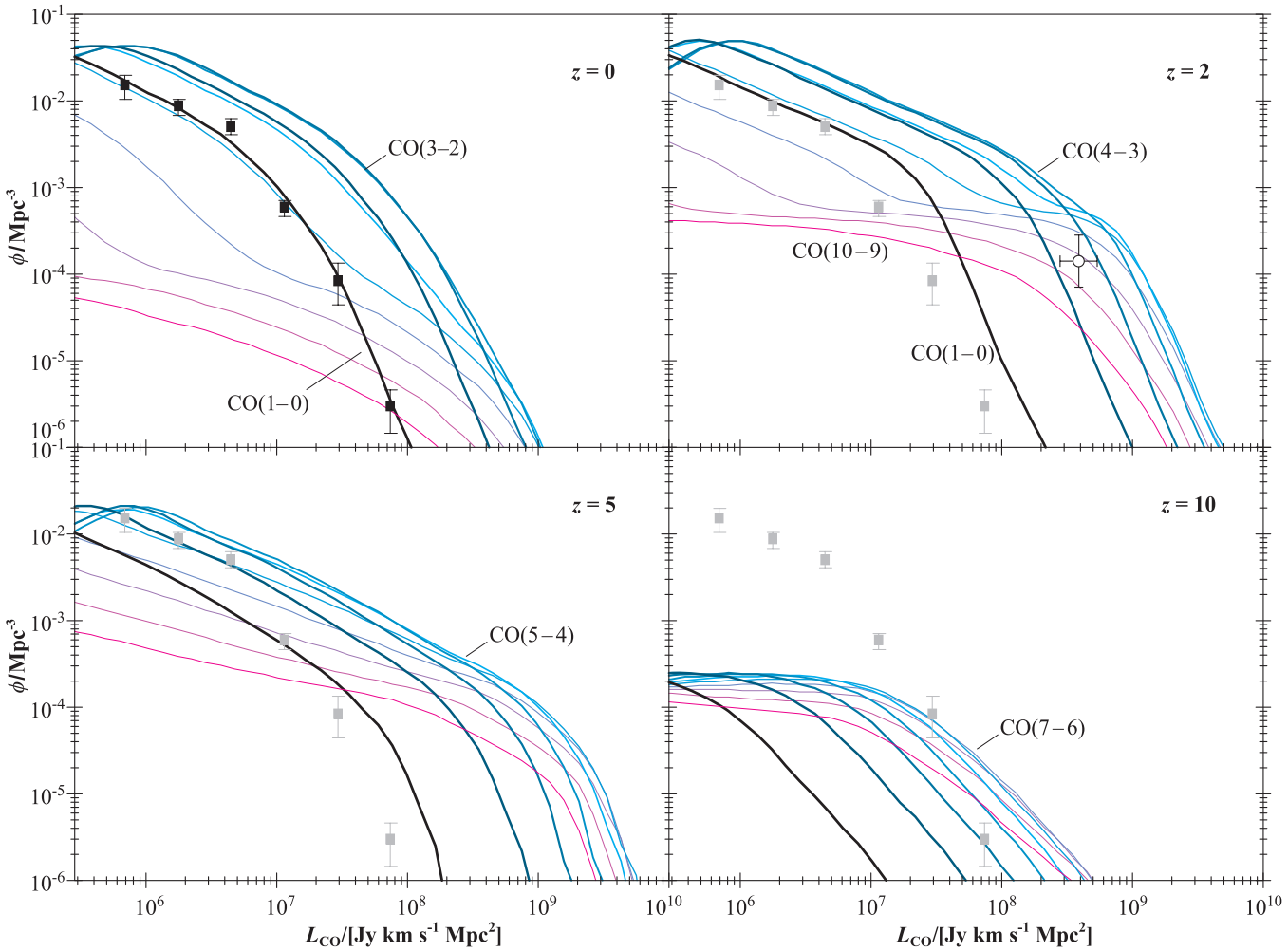

Figure 3. Predicted cosmic evolution of the CO-LFs in the redshift range $z = 0$–10. The thick black line represents the CO(1–0) transition, while increasingly thin and red lines represent the increasingly higher order transitions up to CO(10–9). Filled points and error bars represent the observed CO(1–0) LF of the local universe (Keres et al. 2003). The open circle with error bars corresponds to the CO(2–1) density estimate based on two detections in regular galaxies at $z \approx 1.5$ by (Daddi et al. 2008, see Obreschkow & Rawlings 2009a). The differential space density $\phi(L^{\rm V})$ is defined as the number of sources per unit comoving volume and unit $\log_{10}(L^{\rm V})$ with a velocity-integrated luminosity $L^{\rm V}$.

the HX luminosity scale onto the CO(6–5) luminosity scale, we crudely assumed a proportional relation between the two, tuned to the empirical data from the Cloverleaf quasar. We evaluated the lensed HX luminosity (at 2–8 keV rest frame) of the Cloverleaf quasar directly from the X-ray SED measured and corrected for Galactic absorption by Oshima et al. (2001). For the cosmology of this paper, this HX luminosity is $L_{\rm HX} = (1 \pm 0.5) \times 10^{45}\,{\rm erg\,s^{-1}}$. On the other hand, the lensed CO(6–5) line luminosity of the Cloverleaf quasar, interpolated from the CO(5–4) and CO(7–6) line fluxes presented by Barvainis et al. (1997) and corrected for the standard cosmology of this paper, amounts to $L_{J=6} \approx 5 \times 10^{10}\,{\rm Jy\,km\,s^{-1}\,Mpc^2}$. Assuming that the $L_{\rm HX}/L_{J=6}$ ratio of the Cloverleaf quasar is not affected by differential magnification and that it mimics the $L_{\rm HX}/L_{J=6}$ ratio of local AGNs, the HX LF (Yencho et al. 2009) transforms into the data points shown in Figure 4. The vertical error bars represent the statistical density uncertainties given for the HX LF, while the horizontal error bars represent the 50% uncertainty of $L_{\rm HX}$. The good fit between the space densities of local AGNs and those predicted for the luminous CO(6–5) sources supports our prediction.

At very high redshift ($z \gtrsim 7$), where the predicted space density of AGNs in the DeLucia catalog is extremely low (see Croton et al. 2006), SBs become the dominant source of CO heating as shown in Figure 4 (bottom). This analysis predicts that SB-heated molecular gas disks are the most likely objects to be detected in CO-line emission at $z \gtrsim 7$. The optimal transitions are CO(8–7) and CO(6–5) in terms of velocity-integrated luminosities or surface-brightness temperatures, respectively.

The effects of gas heating by the CMB are discussed together with the effects of the CMB as an observing background in Section 5.5.

5.2. *Effects of Overlapping and Smooth Gas*

The effect of overlapping clumps (Section 3.2) exhibits a modest dependence on the upper J-level of the CO transitions, although minor differences may occur due to the dependence of the optical depths on J (see Equation (5)). Our model predicts that the effect of overlapping clouds becomes increasingly important with redshift, as a direct consequence of the predicted increase in the surface densities of galaxies with redshift. Between $z = 0$ and $z = 1$, the effect is negligible (i.e., < 0.1 dex luminosity change), while at $z = 5$ CO luminosities are predicted to be reduced by a factor 2–3 due to cloud overlap. The dashed line in Figure 5 illustrates the effect of ignoring the overlap of clumps (by forcing $B = 1$) at $z = 5$.

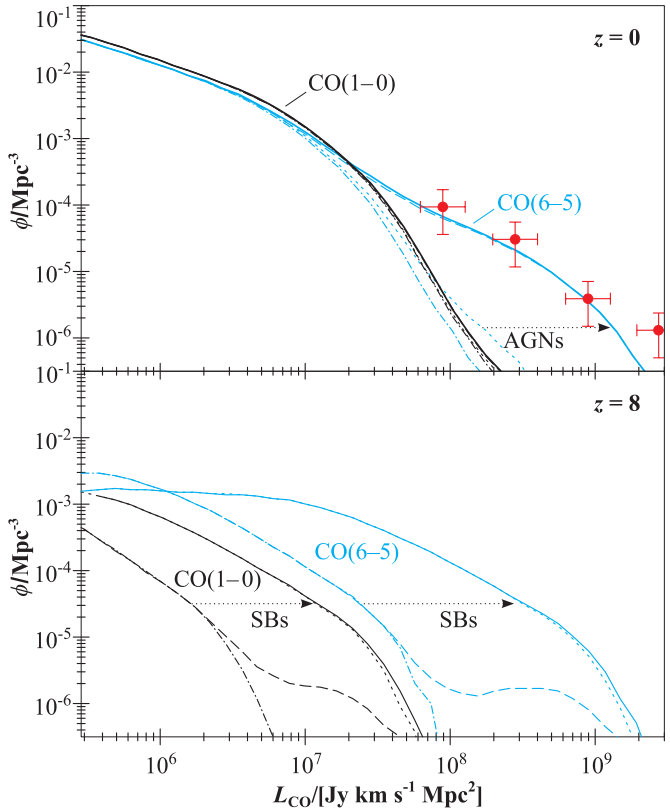

Figure 4. Effects of SB and AGN heating on the CO(1–0) LF (black) and CO(6–5) LF (blue) at redshifts $z = 0$ and $z = 8$. The solid lines represent the CO-LFs of the full model, such as shown in Figure 3, while the other lines represent the cases where either SBs (dashed), AGNs (dotted), or both (dash dotted) were suppressed in the simulation. The red dots with error bars represent the local HX LF (Oshima et al. 2001), mapped onto the CO(6–5) luminosity scale as explained in Section 5.1.

(A color version of this figure is available in the online journal.)

5.3. Effects of Smooth Gas

In our model (see Section 3.3), we assumed that molecular gas in very dense galaxy parts is smoothly distributed, rather than organized in gravitationally bound GMCs. Within our simplistic treatment (Equations (13) and (16)), this effect is independent of the J-level of the CO transition. The effect of smooth gas becomes increasingly important with redshift, as a direct consequence of the predicted increase in the surface densities of galaxies with redshift. Between $z = 0$ and $z = 1$, the effect is negligible (i.e., < 0.1 dex luminosity change), but at $z = 5$ its importance is comparable to that of heating by strong SBs and massive AGNs. The dotted line in Figure 5 shows the effect of ignoring the possibility of smooth gas (by forcing $f_{\rm clumpy} = 1$) at $z = 5$.

5.4. Effects of Metallicity

Figure 6 shows the effect of neglecting the cosmic evolution of cold metals in galaxies, by illustrating the effects at $z = 5$ of suppressing this evolution. In general, the effect of metallicity appears to be relatively weak, since the cosmic evolution of the cold gas metallicity from $z = 5$ to $z = 0$ is relatively weak as discussed in more detail in Section 6.3 of Obreschkow et al. (2009).

We also note that the cosmic evolution of the cold gas metallicity has a stronger effect on weak CO sources than on the luminous ones. In fact, galaxies more luminous than the "knee"

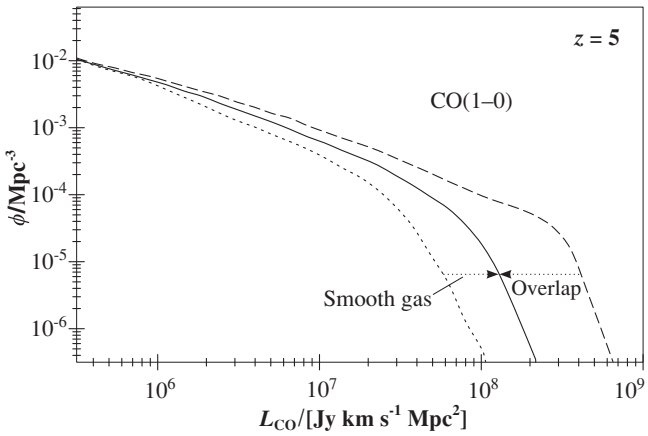

Figure 5. Effects of overlapping clumps and smoothly distributed gas on the CO(1–0) LF at $z = 5$. The solid line represents the CO-LF of the full model, such as shown in Figure 3. The other lines correspond to the suppression of overlap effects (dashed) and smoothly distributed gas (dotted). Note the different scale of the axes compared to the other figures.

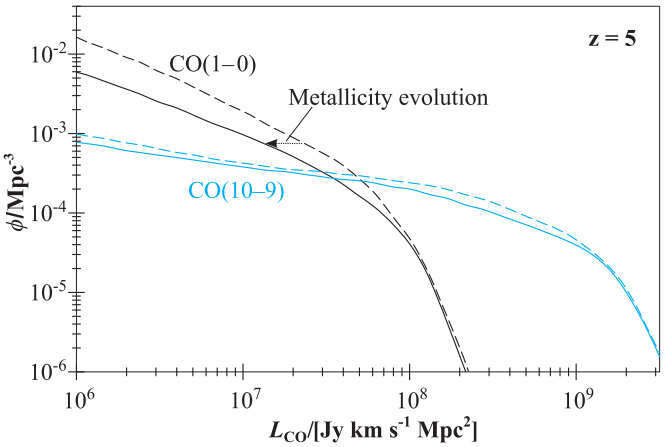

Figure 6. Effects of the cosmic evolution of cold gas metallicity on the LFs of CO(1–0) (black) and CO(10–9) (blue) at $z = 5$. The solid lines represent the CO-LFs of the full model, such as shown in Figure 3, while dashed lines represent the CO-LFs, where the cosmic evolution of metals has been suppressed in the simulation.

(A color version of this figure is available in the online journal.)

of the CO-LFs are nearly unaffected by the cosmic evolution of metals at $z = 5$ compared to $z = 0$. The reason for this feature is that the more CO-luminous galaxies are, on average, more massive and older, and hence they have already formed the bulk of their metals at $z > 5$.

5.5. Effects of the CMB

The CMB as an observing background already becomes noticeable at $z \approx 1$, where its effective reduction of the CO(1–0) luminosities amounts to about 0.1 dex (less for higher order transition) according to Equation (15). This effect increases steeply with redshift and reaches 1 dex at $z \approx 5$ for the CO(1–0) line, such as shown in Figure 7. The increase of the CO excitation temperature by the heating effect of the CMB appears to be a minor effect, which only becomes noticeable around $z \approx 5$. This effect acts against the loss of detectable luminosity by the CMB as an observing background by about 10% at $z \approx 5$ for the CO(1–0) line (slightly more for higher order transitions).

Our model generally predicts that the effect of the CMB as an observing background always dominates the opposite

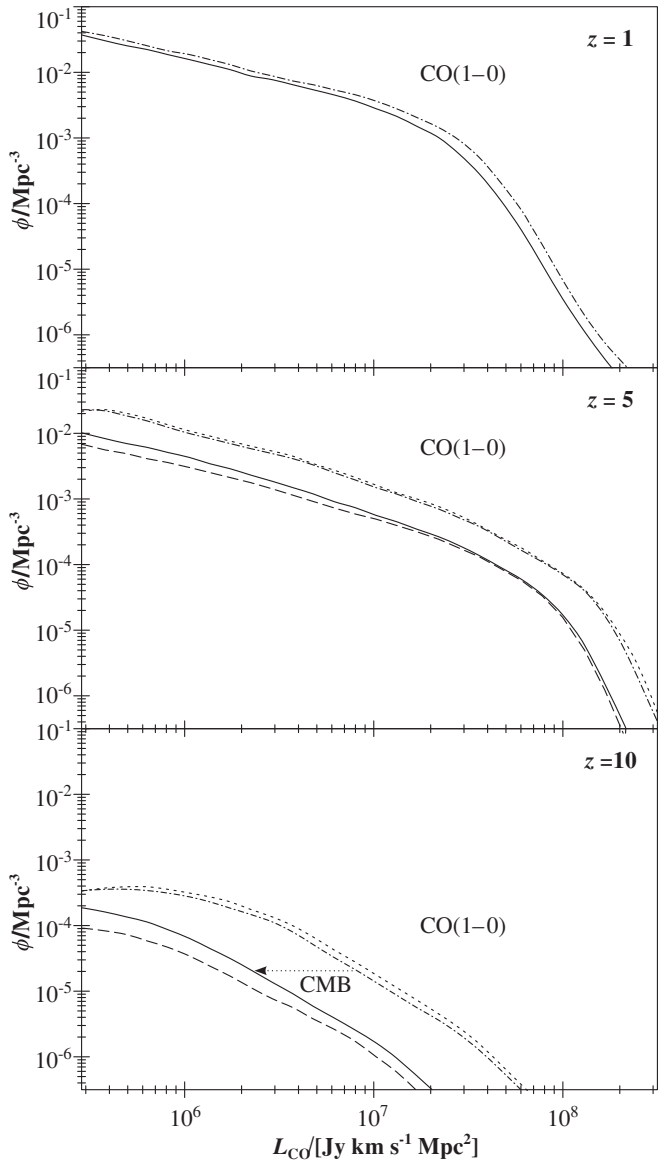

Figure 7. Effects of the CMB on the CO(1–0) LF at $z = 1$, $z = 5$, and $z = 10$. The solid lines represent the CO-LFs corresponding to the full model, such as shown in Figure 3. The other lines represent the cases, where either the gas heating by the CMB (dashed), the CMB as an observing background (dotted), or both effects (dash dotted) have been suppressed in the simulation.

effect of the CMB as a source of heating. Hence, the combined effect of the CMB always reduces the detectable luminosities of CO sources, at all redshifts and for all rotational transitions. This effect is most pronounced for lower order transitions, since emission from higher order transitions originates mostly from SBs and AGNs, whose heating effect can mask the comparatively low temperature of the CMB (e.g., $T_{\rm CMB} \ll T_{\rm SB}$ and $T_{\rm CMB} \ll T_{\rm AGN}$). For regular galaxies (no SBs, no AGNs), the combined effect of the CMB increases with redshift in such a way that these galaxies become virtually invisible in CO-line emission against the CMB at $z \gtrsim 7$.

This result contradicts the claims of Silk & Spaans (1997) and Gnedin et al. (2001) that the higher excitation temperatures caused by the warm CMB of the early universe will ease the detection of CO-emission lines. The conclusion of these authors only accounts for gas heating by the CMB, but it ignores the CMB as an inevitable observing background. The importance of the CMB as an observing background has already been emphasized by Combes et al. (1999) and Papadopoulos et al. (2000).

6. DISCUSSION

6.1. Ranking of Various Mechanisms

The analysis of Section 5 can be summarized in a ranking list of the different mechanisms affecting the CO/H_2 conversion. This ranking naturally depends on the redshift, the considered part of the CO-LF, and the J-level of the CO transition. Here, we consider the source population around the "knee" of the CO-LFs for the levels $J = 3$–6 at redshift $z \approx 3$. This case corresponds to using the fully funded (Maiolino 2008) ALMA-bands 3 and 4 for the first ALMA science goal, i.e., the detection of a MW-type galaxy in CO-line emission at $z \approx 3$ (De Breuck 2005). For this particular setting, the predicted ranking (from most important to least important) is as follows:

1. Gas heating by AGNs (+)
2. Gas heating by SBs (+)
3. Overlap of clumps (−)
4. Smooth gas (+)
5. CMB as an observing background (−)
6. Cosmic evolution of the cold gas metallicity (−)
7. Gas heating by the CMB (+).

The signs in parentheses indicate whether the effect increases (+) or decreases (−) the CO-line luminosities. Although this ranking may change considerably with redshift and with J (e.g., Figure 4), the above ranking can be considered as a rule of thumb for estimating the relative importance of various effects. For example, if a simulation of CO-LFs includes a model for the smooth gas in high-redshift galaxies, then it should also account for the heating by SBs and AGNs and self-shielding by overlapping clumps.

6.2. Model Limitations

The predictions presented is this paper are approximate ramifications of a semiempirical model, which potentially suffers from simplifications and uncertainties on each of the four successive simulation layers: (1) the Millennium dark matter simulation, (2) the semianalytic galaxy simulation of the DeLucia catalog, (3) our postprocessing to assign extended H I and H_2 properties to each galaxy, and (4) the model for CO-line emission introduced in this paper. It is beyond the scope of this paper to discuss the limitations related to the simulation layers (1)–(3), but extensive discussions were provided by Springel et al. (2005), Croton et al. (2006), and Obreschkow et al. (2009), respectively.

All four simulation layers were widely constrained by a broad variety of observations: (1) the cosmological parameters for the Millennium Simulation were adopted from 2dFGRS (Colless et al. 2001) and *WMAP* (Spergel et al. 2003; Bennett et al. 2003); (2) the semianalytic recipes are motivated by various references given in Croton et al. (2006) and the free parameters were tuned to fit the luminosity/color/morphology distribution of low-redshift galaxies (Cole et al. 2001; Huang et al. 2003; Norberg et al. 2002), the bulge-to-black hole mass relation (Häring & Rix 2004), the Tully–Fisher relation (Giovanelli et al. 1997), the cold gas metallicity as a function of stellar mass (Tremonti et al. 2004); (3) our model to assign H I and H_2 properties is motivated by various studies of H I and H_2 in local galaxies (e.g., Young 2002; Blitz & Rosolowsky 2006; Leroy et al. 2008; Elmegreen 1993) and the free parameter was tuned to the local

space density of cold gas (Keres et al. 2003; Zwaan et al. 2005; Obreschkow & Rawlings 2009b); and (4) our CO model was constrained as described in Section 3 of this paper. Since this empirical basis is widely dominated by observations in the local universe, we expect our low-redshift predictions for CO, such as the CO-LFs for higher order transitions, to be more accurate than the high-redshift predictions.

With regard to our model for CO-line emission, the most reliably modeled effects are those of the CMB, since they could be assessed from global considerations, with no strong dependence on free parameters (see Sections 3.5 and 5.1). Also the effects of cold gas metallicity are relatively unproblematic: first, these effects are relatively small (e.g., Figure 6); second, the correlation between metallicity and the CO/H_2 conversion is empirically supported (see Section 3.4); and third, the metallicities predicted by the DeLucia catalog seem reliable as they reproduce the mass–metallicity relation inferred from 53,000 star-forming galaxies in the Sloan Digital Sky Survey (De Lucia et al. 2004; Croton et al. 2006; Tremonti et al. 2004).

The effects of intercloud heating by high-density star formation (or SBs) and heating by AGNs are much less certain. Our temperature model relies on the CO-SEDs of only seven galaxies (four SBs and three QSOs) with poorly constrained star formation densities and black hole accretion rates. It is further possible that the molecular material in some of these galaxies is simultaneously heated by both a SB and an AGN. The relations of Equations (6)–(8) are simplistic parameterizations of our limited knowledge on gas heating by SBs and AGNs, but they may require a revision as larger galaxy samples with simultaneous CO-SEDs, SFRs, and black hole accretion rates come online. Given the present-day uncertainties of SB and AGN heating, the use of the LTE model for CO-SEDs (Section 5.1) seems sufficient. In fact, the offset of the LTE model from the more complex LVG models is small (Combes et al. 1999) compared to the systematic uncertainties of radiative heating by SBs and AGNs.

Surprisingly, we found that self-shielding by overlapping clumps is perhaps the most subtle effect to model at $z > 3$, because it seems to be a very significant effect (see Figure 5) and yet its physical complexity is considerable. Especially, in the case of galaxies with heavily overlapping clumps (i.e., $B \gg 1$), the value of the overlap parameter B sensibly depends on the radius and mass of molecular clumps. If we also consider that clumps are not randomly distributed, but organized in cloud complexes, and that their geometries are far from spherical, the predicted CO-line luminosities of galaxies with heavily overlapping clumps could differ from our current prediction by nearly an order of magnitude. Similar uncertainties should be assumed for the effects of smooth gas in high-redshift galaxies. In fact, the critical surface density Σ_c, at which gas transforms from clouds to smooth disks, is very uncertain and may vary as a function of the mass and size of the galaxy.

7. CONCLUSION

We have predicted the cosmic evolution of the galaxy LFs for the first 10 rotational transitions of the CO molecule. This prediction relies on a combination of a recently presented simulation of H_2 masses in $\sim 3 \times 10^7$ evolving galaxies with a model for the conversion between H_2 masses and CO-line luminosities. The latter model accounts for radiative heating by AGNs, SBs, and the CMB, for smooth and overlapping gas, for the cosmic evolution of metallicity, and for the CMB as an observing background.

The main outcome of this study is twofold. First, the predicted CO-LFs are probably the most robust basis to date toward predicting the CO-line detections of high-redshift surveys with future telescopes, such as ALMA (see Blain et al. 2000) or phase 3 of the Square Kilometre Array (SKA; Carilli & Rawlings 2004). Second, this study revealed that the most serious uncertainties of the CO-LFs at high redshifts originate from the poorly understood self-shielding of overlapping clouds, from the smooth gas in luminous galaxies, and from the heating by SBs and AGNs. Hence, any serious progress in predicting the CO-LFs must address these mechanisms in more detail. By contrast, the widely cited effects of the CMB and the cosmic evolution of metallicity seem to be relatively well modeled.

This study makes some explicit predictions, which could be tested in future CO surveys, e.g.,

1. The CO-LFs associated with the first 10 rotational transitions should show a strong signature of "downsizing" in the redshift range $z = 0$–2. Explicitly, the total power of each CO line per comoving volume increases from $z = 0$ to $z = 2$ by a factor of 2 to more than 10, depending on the CO transition (see Figure 3).
2. On average, the relative CO-line power in higher order transitions, i.e., the excitation temperature T_e, increases monotonically with redshift z. This is a consequence of more heating at high-z, mainly due to SBs and AGNs (see Figure 3).
3. Some CO-LFs (e.g., CO(6–5) and CO(7–6) at $z = 0$, and CO(5–4), CO(6–5), and CO(7–6) at $z = 2$) significantly deviate from a Schechter function. They are predicted to have two "knees," respectively, corresponding to a "normal" galaxy population and a more CO-luminous population, where the gas is heated mostly by AGNs (e.g., Figure 4, top).
4. Out to the most distant galaxies, most of the cosmic CO luminosity is predicted to stem from regular clumpy gas, i.e., from GMCs, rather than a hypothetical dense phase, which is believed to dominate some ULIRGs (Downes et al. 1993; Downes & Solomon 1998).
5. The CMB will significantly suppress the apparent CO-line flux of galaxies at high-z (see Figure 7). In particular, galaxies at $z \gtrsim 7$ with no strong source of internal heating, such as a SB or an AGN, will not be detectable in CO-line emission.

This effort/activity is supported by the European Community Framework Programme 6, Square Kilometre Array Design Studies (SKADS), contract no. 011938. The Millennium Simulation databases and the web application providing online access to them were constructed as part of the activities of the German Astrophysical Virtual Observatory.

APPENDIX A

LUMINOSITIES AND FLUXES OF LINES

This section overviews the concepts used in relation with line fluxes and line luminosities with an emphasis on connecting the terminology and units of observers to those of theoreticians.

A.1. Terminology and Definitions

Any continuous isotropic electromagnetic radiation from a point source is completely characterized by the luminosity density (or monochromatic luminosity) $l(\nu)$, an intrinsic quantity measured in units proportional to $1\,\mathrm{W\,Hz^{-1}} \equiv 1\,\mathrm{J}$.

The corresponding observable quantity is the flux density (or monochromatic flux) $s(\nu)$, measured in units proportional to $1\,\mathrm{W\,Hz^{-1}\,m^{-2}} \equiv 1\,\mathrm{kg\,s^{-2}}$ ($1\,\mathrm{Jy} = 10^{-26}\,\mathrm{W\,Hz^{-1}\,m^{-2}}$).

The luminosity distance D_L is defined in such a way, that the conservation of energy applied to $l(\nu)$ and $s(\nu)$ takes the standard form of the continuity equation,

$$\int l(\nu)d\nu = 4\pi D_\mathrm{L}^2 \int s(\nu)d\nu. \tag{A1}$$

By definition a source is at redshift z, if electromagnetic radiation emitted by this source at a rest-frame frequency ν_e is observed at a frequency $\nu_\mathrm{o} = \nu_\mathrm{e}\,(1+z)^{-1}$; or, in terms of wavelengths, $\lambda_\mathrm{o} = \lambda_\mathrm{e}\,(1+z)$. A frequency interval $d\nu$ around ν_e will be compressed to $d\nu(1+z)^{-1}$, when observed at ν_o; therefore,

$$l(\nu_\mathrm{e}) = 4\pi D_\mathrm{L}^2 s(\nu_\mathrm{o})\,(1+z)^{-1}. \tag{A2}$$

If the source presents an emission line centered at a rest-frame frequency ν_e, one often considers the integrated luminosity and flux from the whole line. However, at least three definitions of these integrated quantities are commonly used. The most physically meaningful choices are the frequency-integrated quantities

$$L \equiv \int_{\nu_\mathrm{e}-\Delta\nu_\mathrm{e}}^{\nu_\mathrm{e}+\Delta\nu_\mathrm{e}} l(\nu)d\nu,\; S \equiv \int_{\nu_\mathrm{o}-\Delta\nu_\mathrm{o}}^{\nu_\mathrm{o}+\Delta\nu_\mathrm{o}} s(\nu)d\nu, \tag{A3}$$

where $\Delta\nu_\mathrm{e}$ and $\Delta\nu_\mathrm{o}$ represent the half-widths of the line in rest-frame frequency and observer-frame frequency, respectively. The precise definition of these half-widths (i.e., the definition of where the line ends) depends on the observer's choice. L represents the actual power of the emission line and is measured in units proportional to 1 W ($1\,L_\odot = 3.839 \times 10^{26}$ W). S represents the power per unit area received by the observer, measured in units proportional to $1\,\mathrm{W\,m^{-2}} \equiv 1\,\mathrm{kg\,s^{-3}}$.

An alternative definition to the frequency-integrated quantities are the velocity-integrated analogs, often preferred by observers,

$$L^\mathrm{V} \equiv \int_{-\Delta V}^{+\Delta V} l(\nu)dV,\; S^\mathrm{V} \equiv \int_{-\Delta V}^{+\Delta V} s(\nu)dV, \tag{A4}$$

where V is the rest-frame velocity, projected on the line of sight, of the emitting material relative to the center of the observed galaxy, and ΔV is the maximal velocity (rotation+dispersion) of the emitting material. L^V is measured in units proportional to $1\,\mathrm{kg\,m^3\,s^{-3}}$ ($1\,\mathrm{Jy\,km\,s^{-1}\,Mpc^2} = 9.521 \times 10^{21}\,\mathrm{kg\,m^3\,s^{-3}}$), and S^V is measured in units proportional to $1\,\mathrm{kg\,m\,s^{-3}}$ ($1\,\mathrm{Jy\,km\,s^{-1}} = 10^{-23}\,\mathrm{kg\,m\,s^{-3}}$).

Confusion sometimes arises in the definition of the velocity V in Equations (A4), since several definitions of velocity are commonly used in the context of emission and absorption lines (see Figure 8): (1) the standard recession velocity $V_\mathrm{opt}(\nu) = c(\nu_\mathrm{e}-\nu)/\nu$, traditionally used by optical astronomers; (2) the variation $V_\mathrm{radio}(\nu) = c(\nu_\mathrm{e}-\nu)/\nu_\mathrm{e}$, sometimes employed by radio astronomers; and (3) the "intrinsic rest-frame velocity" W, representing the rest-frame velocity, projected on the line of sight, of the emitting material relative to the center of the observed galaxy. For the investigation of emission (or absorption) lines at high redshift, it is critical to specify, which definition of the velocity V is used in the definition of velocity-integrated quantities like L^V and S^V. The most natural choice, which we adopted in Equations (A4), is $V = W$. This is the only choice, which makes L^V an intrinsic property, that does not depend on the observer's distance.

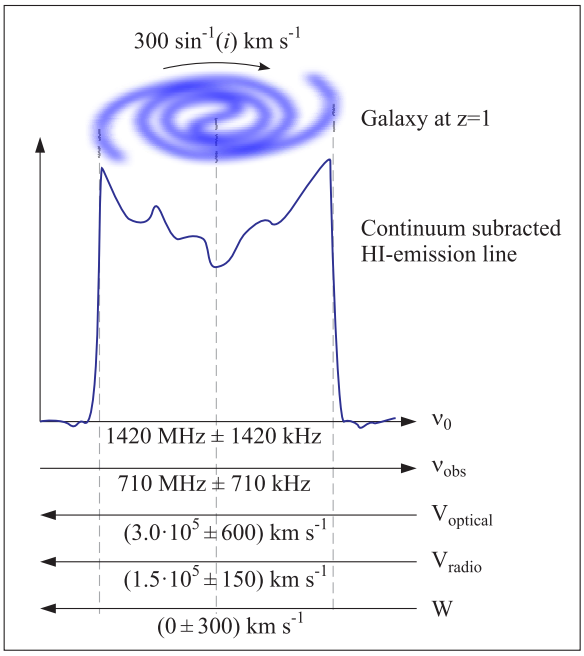

Figure 8. Different velocity measures used in relation to emission lines from galaxies.
(A color version of this figure is available in the online journal.)

In the rest frame of the observed galaxy, the center of the emission line is at the frequency ν_e and V is computed as $V = c(\nu-\nu_\mathrm{e})/\nu_\mathrm{e}$. Hence,

$$\frac{dV}{d\nu} = \lambda_\mathrm{e} \text{ if } \nu \text{ is in the rest frame.} \tag{A5}$$

In the observer's frame, the center of the emission line is at the frequency ν_o and V is computed as $V = c(\nu-\nu_\mathrm{o})/\nu_\mathrm{o}$. Hence,

$$\frac{dV}{d\nu} = \lambda_\mathrm{o} \text{ if } \nu \text{ is in the observer frame.} \tag{A6}$$

Sometimes, line luminosities are defined with respect to the surface-brightness temperature T_B, which is defined as the (frequency-dependent) temperature of a blackbody with the physical size of the observed source and providing an identical flux density $s(\nu_\mathrm{o})$. In radio astronomy, the energy distribution of a blackbody is commonly approximated by the Rayleigh–Jeans law, i.e., the power radiated per unit of surface area, frequency, and solid angle equals $u(\nu) = 2\nu^2 k T_\mathrm{B} c^{-2}$, where k_b is the Boltzmann constant. For isotropic line emission at rest-frame frequency ν_e this implies $l(\nu_\mathrm{e}) = 4\pi D_\mathrm{A}^2 \Omega\, u(\nu_\mathrm{e}) = 8\pi \nu_\mathrm{e}^2 k_\mathrm{b} T_\mathrm{B} c^{-2} D_\mathrm{A}^2 \Omega$, where $D_\mathrm{A} = D_\mathrm{L}(1+z)^{-2}$ is the angular diameter distance and Ω is the solid angle subtended by the source. Using Equation (A2), we then obtain

$$T_\mathrm{B}(\nu_\mathrm{o}) = \frac{c^2}{2\,k_\mathrm{b}} \frac{s(\nu_\mathrm{o})\,\nu_\mathrm{e}^{-2}\,(1+z)^3}{\Omega}. \tag{A7}$$

T_B is an intrinsic quantity, which does not change with redshift z, as can be seen from $s(\nu_\mathrm{o})/\Omega \propto (1+z)^{-3}$. Often the brightness temperature intensity I of an emission line source is defined as the velocity-integrated brightness temperature

$$I \equiv \int_{-\Delta V}^{+\Delta V} T_\mathrm{B}(\nu)dV, \tag{A8}$$

giving units proportional to $1\,\mathrm{K\,m\,s^{-1}}$ ($1\,\mathrm{K\,km\,s^{-1}} = 10^3\,\mathrm{K\,m\,s^{-1}}$). Alternatively, observers sometimes define the intensity I as the velocity integral of the "beam-diluted" brightness temperature $T_{\rm mb}$, which is smaller than $T_{\rm B}$ if the source does not cover the whole beam. We also note that some authors use the symbol I for fluxes, which we label S (e.g., Weiss et al. 2007). The brightness temperature luminosity $L^{\rm T}$ is defined as the product of the intensity and the source area (Solomon et al. 1997)

$$L^{\rm T} \equiv D_{\rm A}^2 \Omega \int_{-\Delta V}^{+\Delta V} T_{\rm B}(v) dV. \tag{A9}$$

This implies that $L^{\rm T}$ is measured in units proportional to $1\,\mathrm{K\,m^3\,s^{-1}}$ ($1\,\mathrm{K\,km\,s^{-1}\,pc^2} = 9.521 \times 10^{35}\,\mathrm{K\,m^3\,s^{-1}}$).

A.2. Basic Relations

From the conservation law of Equation (A1), we directly find the flux-to-luminosity relations

$$L = 4\pi D_{\rm L}^2\, S. \tag{A10}$$

The velocity-integrated flux $S^{\rm V}$ can be expressed in terms of the frequency-integrated flux S by using the Jacobian of Equation (A6)

$$S^{\rm V} = \lambda_{\rm o}\, S. \tag{A11}$$

Similarly, the velocity-integrated luminosities $L^{\rm V}$ can be expressed in terms of the frequency-integrated luminosity L (i.e., intrinsic power of the emission line) by using the Jacobian of Equation (A5)

$$L^{\rm V} = \lambda_{\rm e}\, L. \tag{A12}$$

Finally, from Equations (A7), (A9), (A10), and (A11)

$$L^{\rm T} = (8\pi k_{\rm b})^{-1} \lambda_{\rm e}^3\, L. \tag{A13}$$

Using the four basic relations of Equations (A10)–(A13), we can express any of the quantities L, S, $L^{\rm V}$, $S^{\rm V}$, and $L^{\rm T}$ as a function of any other. For example, Equations (A10), (A11), and (A12) imply that

$$L^{\rm V} = (1+z)^{-1}\, 4\pi D_{\rm L}^2\, S^{\rm V}. \tag{A14}$$

Note that this relation differs from Equation (A10) by a redshift factor. Equations (A10) and (A12) imply that

$$L = \frac{4\pi}{c}\, D_{\rm L}^2 \nu_{\rm o} S^{\rm V}, \tag{A15}$$

or, using typical observer units

$$\frac{L}{L_\odot} = 1.040 \times 10^{-3} \left(\frac{D_{\rm L}}{\rm Mpc}\right)^2 \frac{\nu_{\rm o}}{\rm GHz}\, \frac{S^{\rm V}}{\rm Jy\,km\,s^{-1}}. \tag{A16}$$

This is equivalent to Equation (1) in Solomon & Vanden Bout (2005). Similarly, Equations (A10), (A11), and (A13) imply that

$$L^{\rm T} = \frac{c^2}{2\,k_{\rm b}}\, \nu_{\rm o}^{-2}\, D_{\rm L}^2 (1+z)^{-3} S^{\rm V}, \tag{A17}$$

or, in observer units

$$\frac{L^{\rm T}}{\rm K\,km\,s^{-1}\,pc^2} = 3.255 \times 10^7 \left(\frac{\nu_{\rm o}}{\rm GHz}\right)^{-2} \left(\frac{D_{\rm L}}{\rm Mpc}\right)^2 \times (1+z)^{-3}\, \frac{S^{\rm V}}{\rm Jy\,km\,s^{-1}}, \tag{A18}$$

which is identical to Equation (3) in Solomon & Vanden Bout (2005).

APPENDIX B

BACKGROUND OF THE CO/H_2 CONVERSION

To date, most estimates of molecular gas masses in galaxies rely on radio and (sub)millimeter emission lines of trace molecules, especially on emission lines associated with the decay of rotational excitations of the CO molecule.

It is not obvious that the CO lines trace H_2, and this method has indeed a long history of controversy. From local observations in the MW, it has become obvious that molecular gas resides in loosely connected giant (∼10–100 pc) "clouds," which are generally composed of hundreds of dense "clumps" (∼1 pc), hosting even denser "cores" (∼0.1 pc), where new stars are born (see, e.g., the Orion molecular cloud; Maddalena et al. 1986; Tatematsu et al. 1993). CO-line emission cannot be used as mass tracer of individual clumps and cores, since they are *optically thick* to rotational CO-emission lines as can be inferred from the intensity ratios between different rotational levels (Binney & Merrifield 1998, Chapter 8). However, if averaged over entire clouds or galaxies (typically 10^4–10^7 clouds), CO behaves as if it were *optically thin*, in a sense that individual clumps and cores do not significantly overlap (in space and frequency; Wall 2006), and hence on these large scales CO-line luminosities are expected to become suitable tracers of the molecular mass. Compelling empirical support for this conclusion was provided by the very tight correlation between the virial masses, estimated from sizes and velocity dispersions, and the CO(1–0) luminosities of 273 molecular clouds in the MW analyzed by Solomon et al. (1987).

To convert CO-line luminosities into H_2 masses, it is common to define the X-factors as

$$X_J \equiv \frac{N_{\rm H_2}}{I_J}, \tag{B1}$$

where J is the upper rotational transition $J \rightarrow J-1$, $N_{\rm H_2}$ is to column number density of H_2 molecules (here, we exclude helium), and I_J is the brightness temperature intensity (see definition in Equation (A8)) of the CO($J \rightarrow J-1$) emission line. Alternatively, the CO/H_2 conversion factors are sometimes defined as (Solomon & Vanden Bout 2005)

$$\alpha_J \equiv \frac{M_{\rm H_2}}{L_J^{\rm T}}, \tag{B2}$$

where $L_J^{\rm T}$ is the brightness temperature luminosity (see definition in Equation (A9)) of the CO($J \rightarrow J-1$) emission line. Note that the definitions of $N_{\rm H_2}$ and $M_{\rm H_2}$ in Equations (B1) and (B2) do not include a helium fraction, but some authors (e.g., Downes et al. 1993) include a helium fraction of ∼36% in $N_{\rm H_2}$ and $M_{\rm H_2}$, which makes their values of X_J and α_J 1.36 times larger.

Since $M_{\rm H_2} = D_{\rm A}^2 \Omega N_{\rm H_2} m_{\rm H_2}$, where $m_{\rm H_2}$ is the mass of a H_2 molecule, and $L_J^{\rm T} = D_{\rm A}^2 \Omega I_J$ for all $J \geqslant 1$, we find that the two conversion factors are related by

$$\alpha_J = X_J\, m_{\rm H_2}, \tag{B3}$$

or, in typical observer units

$$\frac{\alpha_J}{M_\odot (\mathrm{K\,km\,s^{-1}\,pc^2})^{-1}} = \frac{1.6 \times 10^{-20}\, X_J}{(\mathrm{K\,km\,s^{-1}\,cm^2})^{-1}}. \tag{B4}$$

From Equations (A12), (A13), (B2), and (B3), it follows that

$$M_{\rm H_2} = \frac{m_{\rm H_2}\, c^2}{8\pi\, k\, \nu_J^2}\, X_J\, L_J^{\rm V}, \tag{B5}$$

where $L'^{\rm V}_J$ and ν_J, respectively, denote the velocity-integrated luminosity and the rest-frame frequency of the CO($J \rightarrow J-1$) emission line. ν_J can be calculated as $\nu_J = J\,\nu_{\rm CO}$, where $\nu_{\rm CO} = 115\,{\rm GHz}$ is the rest-frame frequency of the CO(1–0)-line. Equation (B5) can then be expressed in typical observer units as

$$\frac{M_{\rm H_2}}{M_\odot} = \frac{313\,J^{-2}\,X_J}{10^{20}({\rm K\,km\,s^{-1}\,cm^2})^{-1}} \times \frac{L'^{\rm V}_{{\rm CO}(J\rightarrow J-1)}}{{\rm Jy\,km\,s^{-1}\,Mpc^2}}. \quad ({\rm B6})$$

Other mass–luminosity and mass–flux relations for H_2 commonly found in the standard literature can be derived from Equation (B6) and the basic relations in Section A.2.

Both the theoretical and the empirical determination of this conversion have a long history in radio astronomy, and are still considered highly challenging problems at the present day (see overviews in Maloney & Black 1988; Wall 2007; Dickman et al. 1986). Different methods to measure α_J (or X_J) were summarized by Downes et al. (1993), Arimoto et al. (1996), and Solomon & Vanden Bout (2005). The latter suggest that a sensible average value for the MW is $\alpha_1 = 3.4\,M_\odot\,({\rm K\,km\,s^{-1}\,pc^2})^{-1}$, or $\alpha_1 = 4.8\,M_\odot\,({\rm K\,km\,s^{-1}\,pc^2})^{-1}$, if helium is included in the definition of α_1.

APPENDIX C

LINE EMISSION OF THERMALIZED CO WITH FINITE OPTICAL DEPTH

The rotational states of a diatomic molecule, such as CO, can be represented in the basis $\{|J,m\rangle\}$, where $J \geqslant 0$ is the angular quantum number and $m \in \{-J, ..., J\}$ is the magnetic quantum number. In the absence of external fields, the energy only depends on J via $E_J = h_{\rm p}\,\nu_{\rm CO}\,J(J+1)/2$, where $\nu_{\rm CO} = 115\,{\rm GHz}$ and is the rest-frame frequency of the transition $J = 1 \rightarrow 0$. In local thermal equilibrium (LTE), the occupation probabilities of these energy levels are therefore given by

$$n_J = \frac{g_J}{\mathcal{Z}(T_{\rm e})}\,\exp\left[-\frac{h_{\rm p}\,\nu_{\rm CO}\,J(J+1)}{2\,k_{\rm b}\,T_{\rm e}}\right], \quad ({\rm C1})$$

where $g_J = 2J+1$ are the degeneracies lifted by the quantum number m, $T_{\rm e}$ is the excitation temperature, and $\mathcal{Z}(T)$ is the canonical partition function, which ensures the normalization condition $\sum n_J = 1$. The partition function is approximated to $< 1\%$ for all $T > 10\,{\rm K}$ by

$$\mathcal{Z}(T_{\rm e}) = \frac{2\,k_{\rm b}\,T_{\rm e}}{h_{\rm p}\,\nu_{\rm CO}} - \frac{2}{3}. \quad ({\rm C2})$$

The interaction between a state $|J,m\rangle$ and the electromagnetic field only permits transitions simultaneously changing J by ± 1 and m by -1, 0, and 1. To determine the electromagnetic emission emerging from the three transitions $|J,m\rangle \rightarrow |J-1,m'\rangle$, where $m' \in \{m, m\pm 1\}$, we require a measure of the rates of spontaneous emission from $|J,m\rangle$, induced emission from $|J,m\rangle$, and absorption by $|J-1,m'\rangle$. These rates are effectively described by the Einstein coefficients $A_{J,J-1}$, $B_{J,J-1}$, and $B_{J-1,J}$ (defined in Binney & Merrifield 1998, Chapter 8), which can be calculated directly from the interaction Hamiltonian between the rotational states and the electromagnetic field. From considerations of a gas in LTE it follows that these coefficients are related via $A_{J,J-1} \propto J^3 B_{J,J-1}$ and $g_{J-1}B_{J-1,J} = g_J B_{J,J-1}$. Rieger (1974) showed that $A_{J,J-1}$ scales with J as

$$A_{J,J-1} \propto \frac{J^4}{2\,J+1}, \quad ({\rm C3})$$

and hence

$$B_{J,J-1} \propto \frac{J}{2\,J+1} \quad \text{and} \quad B_{J-1,J} \propto \frac{J}{2\,J-1}. \quad ({\rm C4})$$

Following Binney & Merrifield (1998), the "source function" l_J, which is proportional to the power radiated per unit frequency from the transition $J \rightarrow J-1$ (i.e., the sum of the power from all the transitions $|J,m\rangle \rightarrow |J-1,m'\rangle$) in an optically thick medium, is then given by

$$l_J \propto \frac{n_J\,A_{J,J-1}}{n_{J-1}\,B_{J-1,J} - n_J\,B_{J,J-1}} \propto \frac{J^3}{\exp\left(\frac{h_{\rm p}\,\nu_{\rm CO}\,J}{k_{\rm b}\,T_{\rm e}}\right) - 1}, \quad ({\rm C5})$$

and hence the *frequency-integrated* power in a medium with arbitrary optical depth τ_J is given by

$$\begin{aligned} L_J &\propto J\,l_J\,\left[1-\exp(-\tau_J)\right] \\ &\propto \left[1-\exp(-\tau_J)\right] \times \frac{J^4}{\exp\left(\frac{h_{\rm p}\,\nu_{\rm CO}\,J}{k_{\rm b}\,T_{\rm e}}\right) - 1}, \end{aligned} \quad ({\rm C6})$$

where

$$\begin{aligned} \tau_J(T_{\rm e}) &\propto J^{-1}\,(n_{J-1}\,B_{J-1,J} - n_J\,B_{J,J-1}) \\ &\propto \exp\left(-\frac{h_{\rm p}\,\nu_{\rm CO}\,J^2}{2\,k_{\rm b}\,T_{\rm e}}\right)\,\sinh\left(\frac{h_{\rm p}\,\nu_{\rm CO}\,J}{2\,k_{\rm b}\,T_{\rm e}}\right). \end{aligned} \quad ({\rm C7})$$

From Equation (A13), the brightness temperature luminosity is given by $L'^{\rm T}_J \propto L_J\,J^{-3}$. In the particular case of an optically thick medium ($\tau_J \rightarrow \infty$) and high temperatures ($k_{\rm b}\,T_{\rm e} \gg h_{\rm p}\,\nu_{\rm CO}\,J$), Equation (C6) then implies that $L'^{\rm T}_J$ is independent of J, which is indeed one of the essential properties of brightness temperature luminosities.

REFERENCES

Ao, Y., Weiß, A., Downes, D., Walter, F., Henkel, C., & Menten, K. M. 2008, A&A, 491, 747
Arimoto, N., Sofue, Y., & Tsujimoto, T. 1996, PASJ, 48, 275
Bally, J., Stark, A. A., Wilson, R. W., & Langer, W. D. 1987, ApJ, 312, L45
Bao, Y.-Y., Zhang, X., Chen, L.-E., Zhang, H.-J., Peng, Z.-Y., & Zheng, Y.-G. 2008, Chin. Astron. Astrophys., 32, 351
Barvainis, R., Maloney, P., Antonucci, R., & Alloin, D. 1997, ApJ, 484, 695
Beck, S. C., & Beckwith, S. V. 1984, MNRAS, 207, 671
Bennett, C. L., et al. 2003, ApJS, 148, 1
Binney, J., & Merrifield, M. 1998, Galactic Astronomy (Princeton, NJ: Princeton Univ. Press)
Blain, A. W., Frayer, D. T., Bock, J. J., & Scoville, N. Z. 2000, MNRAS, 313, 559
Blitz, L., & Rosolowsky, E. 2006, ApJ, 650, 933
Boselli, A., Lequeux, J., & Gavazzi, G. 2002, Ap&SS, 281, 127
Bouwens, R. J., Illingworth, G. D., Blakeslee, J. P., Broadhurst, T. J., & Franx, M. 2004, ApJ, 611, L1
Braine, J., Combes, F., Casoli, F., Dupraz, C., Gerin, M., Klein, U., Wielebinski, R., & Brouillet, N. 1993, A&AS, 97, 887
Carilli, C. L., et al. 2002, AJ, 123, 1838
Carilli, C. L., & Rawlings, S. 2004, New Astron. Rev., 48, 979
Cole, S., et al. 2001, MNRAS, 326, 255
Colless, M., et al. 2001, MNRAS, 328, 1039
Combes, F., Maoli, R., & Omont, A. 1999, A&A, 345, 369
Croton, D. J., et al. 2006, MNRAS, 365, 11

Daddi, E., Dannerbauer, H., Elbaz, D., Dickinson, M., Morrison, G., Stern, D., & Ravindranath, S. 2008, ApJ, 673, L21
De Breuck, C. 2005, in Proc. of the Dusty and Molecular Universe: A Prelude to Herschel and ALMA, ESA Special Publication 577, ed. A. Wilson (Noordwijk: ESA)
de Grijs, R. 2001, Astron. Geophys., 42, 4
de Jong, T., Dalgarno, A., & Chu, S.-I. 1975, ApJ, 199, 69
De Lucia, G., & Blaizot, J. 2007, MNRAS, 375, 2
De Lucia, G., Kauffmann, G., & White, S. D. M. 2004, MNRAS, 349, 1101
Dickman, R. L., Snell, R. L., & Schloerb, F. P. 1986, ApJ, 309, 326
Downes, D., & Solomon, P. M. 1998, ApJ, 507, 615
Downes, D., Solomon, P. M., & Radford, S. J. E. 1993, ApJ, 414, L13
Elmegreen, B. G. 1993, ApJ, 411, 170
Gao, Y. 2008, Nature, 452, 417
Genzel, R., et al. 2008, ApJ, 687, 59
Genzel, R., & Stutzki, J. 1989, ARA&A, 27, 41
Giovanelli, R., Haynes, M. P., da Costa, L. N., Freudling, W., Salzer, J. J., & Wegner, G. 1997, ApJ, 477, L1
Gnedin, N. Y., Silk, J., & Spaans, M. 2001, arXiv:astro-ph/0106110
Greve, T. R., Papadopoulos, P. P., Gao, Y., & Radford, S. J. E. 2009, ApJ, 692, 1432
Greve, T. R., & Sommer-Larsen, J. 2008, A&A, 480, 335
Güsten, R., Philipp, S. D., Weiß, A., & Klein, B. 2006, A&A, 454, L115
Häring, N., & Rix, H.-W. 2004, ApJ, 604, L89
Hopkins, A. M. 2007, in ASP Conf. Ser. 380, Deepest Astronomical Surveys, ed. J. Afonso et al. (San Francisco, CA: ASP), 423
Huang, J.-S., Glazebrook, K., Cowie, L. L., & Tinney, C. 2003, ApJ, 584, 203
Israel, F. 2000, in Molecular Hydrogen in Space, ed. F. Combes & G. Pineau Des Forets (Cambridge: Cambridge Univ. Press), 293
Israel, F. P., & Baas, F. 2003, A&A, 404, 495
Kawabe, R., Kohno, K., Ohta, K., & Carilli, C. 1999, in ASP Conf. Ser. 156, Highly Redshifted Radio Lines, ed. C. L. Carilli et al. (San Francisco, CA: ASP), 45
Keres, D., Yun, M. S., & Young, J. S. 2003, ApJ, 582, 659
Kutner, M. L., & Leung, C. M. 1985, ApJ, 291, 188
Leroy, A. K., Walter, F., Brinks, E., Bigiel, F., de Blok, W. J. G., Madore, B., & Thornley, M. D. 2008, AJ, 136, 2782
Lis, D. C., & Schilke, P. 2003, ApJ, 597, L145
Maddalena, R. J., Morris, M., Moscowitz, J., & Thaddeus, P. 1986, ApJ, 303, 375
Maiolino, R. 2008, New Astron. Rev., 52, 339
Maloney, P., & Black, J. H. 1988, ApJ, 325, 389
Nieten, C., Dumke, M., Beck, R., & Wielebinski, R. 1999, A&A, 347, L5
Norberg, P., et al. 2002, MNRAS, 336, 907
Obreschkow, D., Croton, D., De Lucia, G., Khochfar, S., & Rawlings, S. 2009, ApJ, in press (arXiv:0904.2221)
Obreschkow, D., & Rawlings, S. 2009a, ApJ, 696, L129
Obreschkow, D., & Rawlings, S. 2009b, MNRAS, 394, 1857
Omont, A., Petitjean, P., Guilloteau, S., McMahon, R. G., Solomon, P. M., & Pécontal, E. 1996, Nature, 382, 428
Oshima, T., et al. 2001, ApJ, 563, L103
Papadopoulos, P. P., Röttgering, H. J. A., van der Werf, P. P., Guilloteau, S., Omont, A., van Breugel, W. J. M., & Tilanus, R. P. J. 2000, ApJ, 528, 626
Prochaska, J. X., Herbert-Fort, S., & Wolfe, A. M. 2005, ApJ, 635, 123
Rieger, T. J. 1974, J. Quant. Spectrosc. Radiat. Transfer, 14, 59
Rohlfs, K., & Wilson, T. L. 2004, Tools of Radio Astronomy (4th rev. and Engl. ed.; Berlin: Springer)
Scoville, N. Z., Sargent, A. I., Sanders, D. B., & Soifer, B. T. 1991, ApJ, 366, L5
Silk, J., & Spaans, M. 1997, ApJ, 488, L79
Sivia, D., & Skilling, J. 2006, Data Analysis: A Bayesian Tutorial (2nd ed.; Oxford: Oxford Univ. Press)
Solomon, P. M., Downes, D., Radford, S. J. E., & Barrett, J. W. 1997, ApJ, 478, 144
Solomon, P. M., Rivolo, A. R., Barrett, J., & Yahil, A. 1987, ApJ, 319, 730
Solomon, P. M., & Vanden Bout, P. A. 2005, ARA&A, 43, 677
Spergel, D. N., et al. 2003, ApJS, 148, 175
Springel, V., et al. 2005, Nature, 435, 629
Tacconi, L. J., et al. 2006, ApJ, 640, 228
Tatematsu, K., et al. 1993, ApJ, 404, 643
Thompson, T. A., Quataert, E., & Murray, N. 2005, ApJ, 630, 167
Tremonti, C. A., et al. 2004, ApJ, 613, 898
Wall, W. F. 2006, RevMexAA, 42, 117
Wall, W. F. 2007, MNRAS, 379, 674
Weiss, A., Downes, D., Neri, R., Walter, F., Henkel, C., Wilner, D. J., Wagg, J., & Wiklind, T. 2007, A&A, 467, 955
Weiss, A., Downes, D., Walter, F., & Henkel, C. 2005a, A&A, 440, L45
Weiss, A., Walter, F., & Scoville, N. Z. 2005b, A&A, 438, 533
Wielebinski, R., Dumke, M., & Nieten, C. 1999, A&A, 347, 634
Wilson, C. D. 1995, ApJ, 448, L97
Yencho, B., Barger, A. J., Trouille, L., & Winter, L. M. 2009, ApJ, 698, 380
Young, L. M. 2002, AJ, 124, 788
Zwaan, M. A., Meyer, M. J., Staveley-Smith, L., & Webster, R. L. 2005, MNRAS, 359, L30